International Journal of Nanomedicine

Dovepress
open access to scientific and medical research

Open Access Full Text Article

ORIGINAL RESEARCH

Electrospun L-Lysine/Amorphous Calcium Phosphate Loaded Core-Sheath Nanofibers for Managing Oral Biofilm Infections and Promoting Periodontal Tissue Repairment

Yufeng Ling[1], Menglu Duan[1], Wen Lyu[1], Jie Yang[1,2], Yu Liu[1,3], Shuangshuang Ren[1,4], Wenlei Wu[1,3]

[1]Central Laboratory of Stomatology, Nanjing Stomatological Hospital, Affiliated Hospital of Medical School, Research Institute of Stomatology, Nanjing University, Nanjing, People's Republic of China; [2]Department of Periodontology, Nanjing Stomatological Hospital, Affiliated Hospital of Medical School, Research Institute of Stomatology, Nanjing University, Nanjing, People's Republic of China; [3]Department of Senior Specialist, Nanjing Stomatological Hospital, Affiliated Hospital of Medical School, Research Institute of Stomatology, Nanjing University, Nanjing, People's Republic of China; [4]Department of Cariology and Endodontics, Nanjing Stomatological Hospital, Affiliated Hospital of Medical School, Research Institute of Stomatology, Nanjing University, Nanjing, People's Republic of China

Correspondence: Wenlei Wu; Shuangshuang Ren, Tel +025-83620252; +025-83620215, Email wlwu@nju.edu.cn; zjndrenss@163.com

Introduction: Periodontitis, a chronic inflammatory disease prevalent worldwide, is primarily treated through GTR for tissue regeneration. The efficacy of GTR, however, remains uncertain due to potential infections and the intricate microenvironment of periodontal tissue. Herein, We developed a novel core-shell structure multifunctional membrane using a dual-drug-loaded coaxial electrospinning technique (Lys/ACP-CNF), contains L-lysine in the outer layer to aid in controlling biofilms after GTR regenerative surgery, and ACP in the inner layer to enhance osteogenic performance for accelerating alveolar bone repair.

Methods: The biocompatibility and cell adhesion were evaluated through CCK-8 and fluorescence imaging, respectively. The antibacterial activity was assessed using a plate counting assay. ALP, ARS, and RT-qPCR were used to examine osteogenic differentiation. Additionally, an in vivo experiment was conducted on a rat model with acute periodontal defect and infection. Micro-CT and histological analysis were utilized to analyze the in vivo alveolar bone regeneration.

Results: Structural and physicochemical characterization confirmed the successful construction of the core-shell fibrous structure. Additionally, the Lys/ACP-CNF showed strong antibacterial coaggregation effects and induced osteogenic differentiation of PDLSCs in vitro. The in vivo experiment confirmed that Lys/ACP-CNF promotes new bone formation.

Conclusion: Lys/ACP-CNF rapidly exhibited excellent antibacterial activity, protected PDLSCs from infection, and was conducive to osteogenesis, demonstrating its potential application for clinical periodontal GTR surgery.

Keywords: anti-microbial therapy, L-lysine, electrospun membrane, osteogenic, periodontal tissue regeneration

Introduction

Periodontal infection is an inflammatory condition of the oral cavity caused by dental plaque.[1] This includes gingivitis, a localized infection of the gingiva that can be reversed with proper oral hygiene, and periodontitis, a more widespread and deep-seated inflammation that can affect multiple organs. If left untreated, periodontitis can lead to adult tooth loss.[2,3] The current gold standard Guided Tissue Regeneration(GTR) membranes used in clinical settings act as a cellular barrier, providing a space for tissue regeneration and reconstructed tooth surrounding tissue. However, bacterial remnants after mechanical removal procedures have the potential to rapidly proliferate and establish biofilms, as well as the bacteria in open oral cavity. This can compromise the capacity of stem cells to repair periodontal complex by inducing the local inflammatory response, which is still widely explored by researchers to alternative materials for GTR membranes that can control biofilm formation and reduce inflammation.[4–6]

Received: 16 January 2024
Accepted: 12 March 2024
Published: 20 March 2024

Graphical Abstract

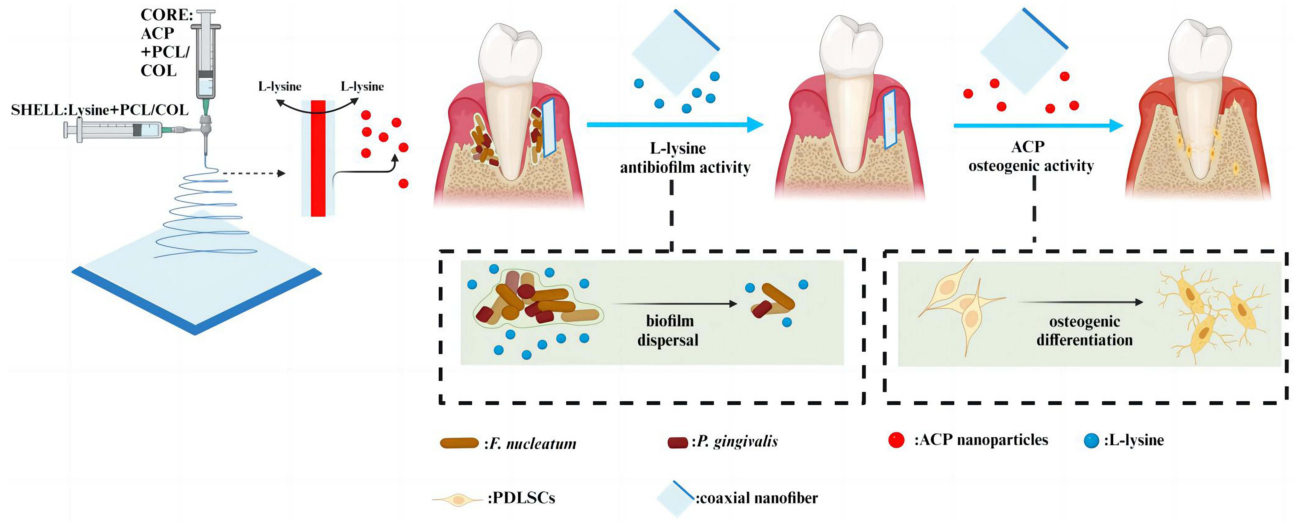

At the clinic, scientists have conducted extensive research to explore potential solutions for the growing issue of dysbacteriosis, poor biodistribution and antibiotic resistance.[7–9] This involves identifying specific bacterial species that play key roles in the development of periodontitis and focusing on achieving efficient clearance of these particular species. One of such prevalent species found in dental plaque is *F.nucleatum(F.n)*, which contains several adhesins such as Fap2, RadD and Aid1 that enable it to interact and co-aggregate with other microbial species present in the oral cavity, such as *Streptococci, Lactobacilli*, and *P.gingivalis*(*P.g*).[10–12] Research has shown that d-amino acids can not only prevent the formation of biofilms but also break down already-formed biofilms.[13,14] Our previous bioinformatics analysis revealed that the gene responsible for L-lysine (Lys) synthesis (FN1461) exhibited lower expression in the *F.n* biofilm compared to the planktonic mode, while the genes involved in Lys degradation (FN1868 and FN1869) demonstrated higher expression,[15] which reveals the potential application of it in inhibiting the formation of dental biofilms.

Periodontal ligament stem cells(PDLSCs) have been shown to have abilities in multiple differentiation including osteogenesis, adipogenesis, chondrogenesis and neurogenesis.[16] When implanted under the skin of immunodeficient mice for 8 weeks, three-phase structure that is similar to the periodontal complex had been observed, suggesting the suitability of PDLSCs in repairing periodontal tissue.[17–19] Calcium phosphate-based drug delivery systems has a distinct advantage in inducing stem cell differentiation in hard tissues and playing a vital role as effective carrier for cytokines. Calcium phosphate also has favorable bioactivity, biocompatibility, and biodegradability, making it widely used in the biomedical field, including amorphous calcium phosphate(ACP)[$Ca_3(PO_4)_2{\cdot}3H_2O$],tricalcium phosphate(TCP)[$Ca_3(PO_4)_2$] and hydroxyapatite(HA) [$Ca_{10}(PO_4)_6(OH)_2$].[19,20] Research shows that the degradation products of ACP have alkaline properties, which can neutralize the surrounding environment.[21,22]

Thus, both Lys and ACP have advantages in periodontal therapy, it is essential to develop a biomaterial system to prevent potential infections and promote periodontal tissue repair, a new drug-loading GTR membrane might be a proper method.[23] As we know, electrospinning is the initial method used for preparing nanofibers. On one hand, it has evolved from a single-fluid blending process to multiple-fluid processes such as coaxial,[24,25] tri-axial, side-by-side[26] and other multiple-fluid process for creating coreshell,[27] Janus,[28] and combined nanostructures.[29–31] On the other hand, electrospun nanofibers are constantly being used in new and innovative applications due to their ability to encapsulate active ingredients for specific purposes.[32–34] Additionally, it is easy to load multiple active ingredients into complex electrospun structures with the ability to tailor components, compositions, and spatial distributions within nanofibers.[35] As a result, this is a powerful method for achieving multiple functional benefits and achieving a designed synergistic effect.[36] The hydrophilic

core can also dissolve to create pores in the sheath, serving as a protective outer layer when the drugs are loaded into the core.[37] We chose Poly(ε-caprolactone) (PCL) and Type I collagen (COL) as the ideal materials for electrospinning due to their exceptional biocompatibility and biodegradability. The flexibility of PCL has been utilized to improve the ductility and fracture strain of nanofibers made of only inorganic materials.[30] Additionally, COL, the primary component of cementum's extracellular matrix, can be incorporated into the nanofibers,[38,39] promoting tissue regeneration, as those fibers with favorable biocompatibility and minimal immunogenicity, facilitate stem cells' adhesion, support and protection.[40]

Thus, we constructed a multi-functional core-sheath nanofibrous membrane as a local drug delivery system (Lys/ACP-CNF) for the therapy of periodontitis with potential post-infection in GTR (table of content image, TOC). Drug release from Lys/ACP-CNF was investigated along with the membrane biodegradation. The antibacterial activity had been enhanced and antibiotic resistance was reduced after Lys was incorporated in the shell layer, which could also facilitate bone regeneration with ACP in the core layer of Lys/ACP-CNF. We proposed that Lys/ACP-CNF, prepared by integrating L-lysine and ACP, the physical and mechanical examinations had been conducted, assessed favorable biocompatibility, anti-bacterial and anti-biofilm effects, and improved osteogenic properties of PDLSCs. Furthermore, rat models of periodontal defect with bacterial infection were constructed to investigate the potential therapeutic effects of Lys/ACP-CNF for GTR and found the exhibited promoted ability on bone regeneration. Herein, we fabricated dual drug-loaded coaxial fibers with dual drug-loading properties, which have the potential to prevent infection and promote periodontal tissue regeneration as GTR mats.

Experimental and Method

Synthesis of ACP Nanoparticles

We prepared a solution containing equal weights of PEG and $CaCl_2$, at a concentration of 0.1 M in 200 mL of water. Next, we dissolved $Na_3PO_4 \cdot 12H_2O$ in 100 mL of distilled water, stirring until fully dissolved. The solution was then stored at 4°C until the temperature stabilized. After that, we combined the two solutions and stirred them magnetically for 30 minutes. The solution was then filtered, washed, and the Cl^- ions were removed until no precipitate was detected through silver nitrate titration. The mixture was frozen for 48 hours and then dried in a dryer as a backup. The resulting nanomedicine particles were weighed and referred to as ACP nanoparticles (ACP).

Characterization of ACP

Fourier Transform Infrared Spectrometer(FTIR)

The FTIR method was used to measure transmittance using a pellet made of potassium bromide (KBr). The spectrum was acquired within the range of 400 cm^{-1} to 4000 cm^{-1}, with a resolution of 4 cm^{-1}, and resulted from 128 scans. Additionally, FTIR was utilized under the same condition for core-sheath nanofibers.

X-Ray Diffraction(XRD)

Approximately 50 mg of ACP was placed into 10 mL of phosphate-buffered saline (PBS) and incubated at 37°C for 1, 2, 3, and 4 weeks. After incubation, the samples were removed, washed, and dried.The specimens' XRD patterns were acquired employing an X-ray tube with a voltage of 40 kV and a current of 40 mA. The specimens were scanned at a rate of 0.1 per second. Following the electrospun material preparation, it was subjected to multiple rinses with deionized water and then freeze-dried. The dried film material was then cut into 1.0cm × 1.0 cm pieces and placed in a holder on a frame. The XRD patterns of the core-sheath nanofiber specimens were obtained under the same condition above.

Transmission Electron Microscopy(TEM)

TEM was used to analyze the structural characteristics of ACP (with or without PEG). The specimens were deposited on carbon-coated copper grids attached to the collector. Electron beams were transmitted through the specimens on the copper grids, and the resulting TEM images of the samples were obtained. TEM was also used to analyze the structural characteristics of core-sheath nanofibers. Specimens were prepared by attaching carbon-coated copper grids to the collector and applying a thin coating of electrospun fibers onto the grid. The copper grids with the fibers were then imaged using TEM by passing electron beams through them.

Fabrication and Characterization of Electrospun Core-Sheath Nanofiber

The COL and PCL were obtained from Sigma (USA), while Lys was acquired from Macklin (China). A spinning solution containing a 1:1 ratio of COL and PCL was prepared using HFIP as a solvent and a solute concentration of 18% (w/v). This created shell and core solutions. L-Lysine was added to the shell solutions, while pre-prepared ACP was added to the core solutions. In the control group, PBS was used as the solvent for the aqueous phase. A coaxial electrospinning needle was connected to two independent core-shell solution injectors. The inner tube diameter was 0.27 mm and the outer tube diameter was 0.17 mm, respectively.Separate pumps were used to deliver the solutions at rates of 0.5 mL h^{-1} (core solution) and 5 mL h^{-1} (shell solution). During the coaxial electrospinning process, a high-voltage power supply was used to generate a 15 kV voltage. The separation distance between the coaxial nozzle and the aluminum foil substrate was kept at a constant value of 13 cm. The thickness of the core-sheath nanofiber was determined by the duration of the electrospinning process, estimated to be approximately 1 mm. All samples were collected on aluminum foil and allowed to air-dry for 48 hours at room temperature to remove any remaining solvents before further analysis. Before each experimental procedure, the nanofibers were exposed to Ultraviolet(UV) radiation for 2 hours, sterilized for an equivalent amount of time with 75% ethanol, dried in a sterile environment, and then washed three times with PBS to remove any remaining ethanol residue.

Scanning Electron Microscope(SEM)

The morphology of the electrospun core-sheath nanofibers was examined using SEM at an accelerating 15 kV voltage. Before observation, the sample surfaces were coated with thin layers of gold through sputter-coating. The analysis of electrospun core-sheath nanofiber diameters and distributions was conducted using Image J analysis software(National Institutes of Health, USA).

Water Contact Angle(WCA)

The hydrophobicity of Lys/ACP-CNF and P-CNF was determined by assessing their water contact angle. This was done at room temperature using the sessile drop method with a Rame-Hart instrument (HARKE-SPCA Contact Angle Measuring instrument, KRUSS DSA100S). A droplet size of 0.5 mL was used. The results were recorded by immediately applying distilled water to the electrospun samples (n=3).

Mechanical Properties

The mechanical properties of the 10×50 mm core-sheath nanofiber were evaluated using an Instron 3340 universal materials tester (Boston, MA, USA). Each sample was subjected to a consistent tensile rate of 10 mm/min, starting from an initial length of 30 mm. The stress-strain curves and Young's moduli were then calculated.

Thermogravimetric Analysis(TGA)

TGA were conducted using a TG 2950 (German - Nexion −209F3A) instrument in a nitrogen atmosphere with a flow rate of 30 mL/min. Around 5 mg of P-CNF, ACP-CNF, Lys-CNF, and Lys/ACP-CNF samples were heated gradually from room temperature to 800 °C at a rate of 10°C/min.

The Controlled Release Assay of L-Lysine and ACP from Lys/ACP-CNF

To assess the release kinetics of L-lysine and ACP from the scaffolds, samples were placed in 24-well plates containing 2.0 mL of PBS (pH 7.4) and agitated in a shaker bath at 37°C and 120 rpm. For L-lysine, the supernatant was collected at predetermined intervals of 1, 4, 6, 7, 9, 12, 15, and 20 days. The collected medium was then replaced with fresh PBS for further quantitative evaluation using the wet method. To track the release of ACP from the central part of the scaffold, samples were placed in 24-well plates filled with deionized water. After 1, 2 and 3 weeks of incubation, the samples were retrieved, dried, and analyzed using EDS to determine the concentration of calcium and phosphate ions.

Human PDLSCs Isolation and Cell Culture

Collect teeth from 18-year-old patients who require orthodontic extraction, but do not have caries or periodontal disease, at the clinic.We also obtained written informed consent from the patients for this study. This study was conducted in accordance with the Declaration of Helsinki and also approved by the Ethics Committee of Affiliated Stomatology

Hospital at Nanjing Medical University (NJSH-2023NL-42).Scrape 1/3 of the periodontal membrane tissue from the root, and cut it into small pieces measuring 1 mm x 1 mm. Put the pieces in small culture bottles. Invert the bottles into an incubator set to 50 mL/L carbon dioxide at a constant temperature of 37°C and incubate for 4 hours to allow the tissue to adhere to the wall. Afterward, add 3 mL of culture medium and change the liquid every 2–3 days. Discard tissue blocks that have not adhered to the wall. When cell growth reaches 80%, transfer the 3rd and 4th generation cells and combine them before inoculating them in a culture plate at a certain cell density.

EDU Labeling Assay

In the EdU labeling assay, PDLSCs were cultured in 6-well plates and incubated for 72 hours. Afterward, a 50 μM EdU labeling medium was added to each well without exposure to light, for 2 hours. The cells were then immobilized, subjected to Hoechst33342 staining, and observed using confocal laser scanning microscopy (CLSM; A1R, Nikon, Japan) for visualization. Images were captured for further analysis.

PDLSCs Morphology on the Frameworks

The morphology of PDLSCs on coaxial electrospun nanofibers was evaluated using CLSM. The cells were cultured on the nanofibers at a concentration of 2.0×10^4 cells per square centimeter and incubated for 72 hours. After removing the cell culture medium, the substrates were washed three times with PBS. Then, they were fixed with 4% paraformaldehyde (Sigma, USA) for 10 minutes at room temperature. Following fixation, the cellular samples were permeabilized using a 0.1% solution of Triton X-100 (Sigma, USA) in PBS for 5 minutes and then incubated in a blocking solution (PBS containing 1% bovine serum albumin (BSA, Sigma, USA)) for 1 hour at room temperature. The treated specimens were then incubated with a 1: 200 dilution of phalloidin conjugated to Alexa Fluor 488 (Invitrogen, Carlsbad, CA, USA) in a light-free environment for 30 minutes. Afterwards, the specimens were stained with 4′,6-diamidino-2-phenylindole (DAPI, Abcam, Cambridge, UK) for 5 minutes in the absence of light. Finally, the specimens were washed six times with PBS before being examined using CLSM.

Live/Dead Staining

To assess cell viability using a Live/Dead staining assay, 10^5 PDLSCs were seeded on core-sheath nanofibers and incubated for 72 hours, then stained at 37 °C for 30 minutes. Calcein-AM from Sigma-Aldrich (St. Louis, MO, USA) was used to label live cells, while dead cells were labeled with Propidium Iodide (Thermofisher, Waltham, MA, USA). After three washes with PBS, the samples were visualized using CLSM.

SEM

To directly assess the morphology and elongation of cells, we gathered samples at intervals of 1, 3, 5, and 7 days post-culturing. Afterward, the samples underwent a PBS wash and were subsequently immersed in a 4% paraformaldehyde solution for a duration of 24 hours at 4 °C. After this, the core-sheath nanofibers were desiccated through a series of ethanol rinses and vacuum freeze-dried for an additional 24 hours. Once dried, the specimens were observed.

Cell Cytocompatibility

PDLSCs were seeded onto P-CNF and Lys/ACP-CNF on 24-well plates. The control group consisted of cells grown on HA. The proliferation of PDLSCs was monitored for 1, 3, 5, and 7 days using a CCK-8 assay. After incubating for 2 hours at 37°C, the absorbance at 450 nm was measured using a microplate reader.

In vitro Antibacterial Activity

Bacterial Strains, Media, and Growth Conditions

The *F.n* (ATCC 25586) and *P.g* (ATCC 33277) were cultivated by initiating growth on Blood Agar Oxoid No. 2 plates supplemented with 5% (v/v) pure sheep blood (Oxoid), 5.0 mg/L of hemin (Sigma, St. Louis, MO, USA), and 1.0 mg/L of vitamin K (Hopebio, Qingdao, China). This cultivation process occurred in (10% H2, 10% CO2, and balanced N2) anaerobic conditions at a temperature of 37 °C for a duration of 3–5 days. Subsequently, colonies were selected, and cultures were further developed in a substrate containing brain-heart infusion(BHI)(Hopebio, Qingdao, China),

supplemented with 5.0 mg/L of hemin and 1.0 mg/L of vitamin K (Hopebio, Qingdao, China), until they reached the exponential growth phase.

The Antibiofilm Activity of Lys/ACP-CNF on *F.n* Mono-Species Biofilm, *F. n* and *P. g* Dual-Species Biofilm

The impact of Lys/ACP-CNF on the biofilm formed by a mono-species of *F. n* was assessed through crystal violet staining method. Initially, *F.n* was introduced at a concentration of 10^8 CFU/mL into 24-well plates containing a control, P-CNF, and Lys/ACP-CNF for biofim formation in anaerobic conditions at a temperature of 37 °C for 24 hours. The wells were subjected to three washes with PBS to eliminate bacteria that did not adhere. Afterwards, they were allowed to air-dry for a duration of 20 minutes, followed by fixation using 2.5% glutaraldehyde for 15 minutes. Subsequently, staining was carried out using 0.1% (wt/vol) crystal violet (Solarbio, Beijing, China) for 15 minutes at room temperature. Any excess dye was removed through washing with PBS, and each well was decolorized with 95% ethanol. The decolorized content was transferred to a 96-well plate and measurements were taken at a 490 nm wavelength.To evaluate the anti-biofilm activity of Lys/ACP-CNF against *F.n* and *P.g* dual-species biofilm, *F.n* was co-cultured with *P.g* at concentrations of 10^6 CFU/mL and 10^8 CFU/mL in 24-well plates with control, P-CNF, and Lys/ACP-CNF for biofim formation in anaerobic conditions at a temperature of 37 °C for 48 hours, using the same crystal violet staining protocol mentioned above.

SEM

We used SEM to observe biofilms of single-species *F.n* and dual-species *F.n* and *P.g*. The specimens were treated with control, P-CNF,and Lys/ACP-CNF for biofim formation in anaerobic conditions at a temperature of 37 °C for 24 hours, followed by post-fixation in 4% paraformaldehyde at 4°C for 24 hours. After that, the samples underwent three washes with PBS and were subjected to dehydration using a sequence of graded ethanol solutions. Subsequently, they were dried, coated with a layer of gold, and subjected to observation.

Measurements of Extracellular Polysaccharide(EPS) by the Phenol-Sulfuric Acid Method

The study evaluated how Lys/ACP-CNF affects the production of EPS in biofilms of *F.n* and *P.g*, both individually and together. The biofilms were cultured under the previously mentioned conditions(2.6.2) and the samples were inoculated at 24,36,48 hours. The *F.n* and *P.g* dual-species biofilm were also cultured under the previously mentioned conditions (2.6.2) and the samples were inoculated at 24,48,72 hours. The biofilms subsequently underwent three washes with PBS. After that, a solution containing 10% phenol and 97% sulfuric acid was introduced and allowed to stand for 10 minutes at ambient temperature. The absorbance at 490 nm was quantified for EPS assessment.

Plate Counting Assay

A study was undertaken to evaluate the survival rate of Lys/ACP-CNF in comparison to *F.n*. A suspension of *F.n* was divided into three groups: control, P-CNF, and Lys/ACP-CNF, and then incubated for 24hours in anaerobic conditions at a temperature of 37 °C for biofilm formation. The diluted bacterial suspensions were then spread onto blood agar plates and cultured for 12 hours. For comparison, untreated bacteria was used as the control substrate. A second experiment as conducted to evaluate the viability of Lys/ACP-CNF when exposed to planktonic forms of *F. n* and *P. g*. Bacterial suspensions were incubated at 37°C for 48 hours in anaerobic conditions at a temperature of 37 °C for biofilm formation and then spread onto blood agar plates for an additional 24 hours.

The Antibacterial and Antibiofilm Activity of Lys/ACP-CNF on *F. n*, *F. n* and *P. g* in Planktonic State

To examine the impact of Lys/ACP-CNF on *F.n* we used a Microplate Reader to measure the absorbance of bacterial growth every 8 hours in 96-well plates. The control group consisted of concentrations of 10^6 CFU/mL of *F.n* each well, and we also included P-CNF and Lys/ACP-CNF over a period of 24 hours for biofilm formation. The *F.n* growth curves under different groups were then plotted.

In another experiment, we assessed the antibacterial properties of Lys/ACP-CNF on planktonic *F.n* and *P.g*. These bacteria were co-cultured in 96-well plates (100 μL/well) with concentrations of 10^6 CFU/mL of *F.n* and 10^8 CFU/mL of

P.g over a period of 72 hours for biofilm formation. We also included control, P-CNF, and Lys/ACP-CNF in this experiment.

Analysis of Biofilm Structure by CLSM

The architecture of *F.n* mono-species biofilm and the dual-species biofilm of *F.n* and *P.g* were examined using CLSM. The biofilms were developed by inoculating 10^8 CFU/mLin 24-well plates containing control, P-CNF, and Lys/ACP-CNF, and were then incubated for 24 hours in anaerobic conditions at a temperature of 37 °C for biofilm formation. The *F.n* mono-species biofilm was washed three times with a sodium chloride solution to remove non-adherent bacteria. It was then stained using the LIVE/DEAD Bacterial Viability Kit (Molecular Probes, Thermo Scientific, USA). Following this, the sample was dual-stained with SYTO 9 and PI at a 1:1 ratio in the absence of light for 15 minutes. After gentle washing with sodium chloride solution, the specimens were positioned inverted in a confocal observation cuvette for the assessment using CLSM (SYTO 9: 515e530 nm; PI: >600 nm). Additionally, the *F.n* and *P.g* dual-species biofilm was created by co-cultivating *F.n* at a concentration of 10^6 CFU/mL with *P.g* at a concentration of 10^8 CFU/mL in 24-well plates with control, P-CNF and Lys/ACP-CNF for 24 hours in anaerobic conditions at a temperature of 37 °C for biofilm formation respectively. This was also analyzed using the CLSM mentioned above.

Alizarin Red S(ARS) Staining Assay

After being stimulated for bone growth for 7 and 14 days, the PDLSCs were washed three times with PBS and then fixed in 70% ethanol for an hour at room temperature. Next, 300 μL of ARS staining solution was added to each well to detect mineral deposits. The background was then washed with PBS until it became transparent. The specimens were then rinsed with PBS until the supernatant was clear, followed by a 1-hour treatment with 10% CPC. The amount of calcium ions discharged in the CPC solution was measured at a 562 nm wavelength.

Alkaline Phosphatase(ALP) Quantitative Evaluation

After being induced for osteogenic activity for several days,the alkaline phosphatase activity was measured in PDLSCs containing different groups of core-sheath nanofibers for 7 and 14 days. This was done by using the ALP Assay Kits following the manufacturer's protocol and instructions. To obtain protein samples, 250 μL of Western and IP cell lysates were added to each well for a few minutes, and then the supernatant was separated by centrifugation. The samples and solutions were then placed into a 96-well plate and incubated at 37°C for 10 minutes in the absence of light. Ultimately, 100 μL of stop solution was added into each well, halting the reaction and producing varying shades of yellow. The absorbance at 405 nm was then assessed.

Reverse Transcription Quantitative Polymerase Chain Reaction(RT-Qpcr) Analysis

Total RNA was carried out using TRIzol®Reagent (Ambion, Life Technologies, Carlsbad, CA, USA) in accordance with the guidelines provided by the manufacturer.The entire RNA pool was then used to generate complementary DNA (cDNA) with the HiScript III 1st Strand cDNA Synthesis Kit (R312-01, Vazyme, Nanjing, China) for subsequent sequencing. RT-qPCR was executed using iQTM SYBR Green Supermix (Q511-02, Vazyme, Nanjing, China) along with custom-designed primers specifically created for this study (refer to Table 1 for primer details).Relative transcription levels were determined using the $2^{-\Delta\Delta t}$ method.

Preparation of the Rat Periodontal Defect Model

To investigate the effectiveness of Lys/ACP-CNF in periodontal regeneration, a rat model with a periodontal defect was established following a previous study.[41] Thirty-two male Sprague-Dawley rat(SD rats), weighing between 100–120 grams, were selected from the Institute of Laboratory Animal Center at Nanjing Agricultural University and given one week to acclimate. This experiment was conducted in accordance with the Declaration of Helsinki.All experimental procedures adhered to the Laboratory Animal Protection Law and were approved by the Ethics Committee and the Animal Care and Use Committee of Nanjing Agricultural University (Approval Code: PZW2023039). Using a standardized method, acute periodontal defects of specific size were created on both sides of the maxilla in the rats. The 64 defect sites were randomly divided into four groups (n=4): (1) Defect, (2) Defect +10^8 *F. nucleatum* injection for 3 days, (3) Defect +10^8 *F. nucleatum* injection for 3 days + Lys-CNF, and (4) Defect +10^8 *F. nucleatum* injection for 3 days + Lys/ACP-CNF. The fibrous material was first disinfected overnight with UV irradiation. After administering

Table 1 The Primer Sequences for RT-qPCR Amplification

GENE	Reverse sequence 5–3'	Forward sequence 5'-3'
16s	ACTGTTAGCAACTACCGATGT	TGTAGATGACTGATGGTGAAA
RadD	ACTATTCCATATTCTCCATAATATTTCCCATTAGA	GGATTTATCTTTGCTAATTGGGGAAATTATAG
FN0669	GTCCACCTGAAAGCTCTGATATT	GAGTTTGATGGCACTTGTAGGA
FN0634	CAGAACCAGCTGCTCTCATATT	GGTTCCAGGTCAAGATGGTTAT
hagA	CGAATTCATTGCCACCTTCT	ACAGCATCAGCCGATATTCC
hagB	CTGGCTGTCCTCGTCGAAAGCATAC	TGTCGCACGGCAAATATCGCTAAAC
RapA	CTACCAGCCCGTTTCCAACT	CTGCGAGCGGTATTAGTGGT
GAPDH	TGGTGAAGACGCCAGTGGA	GCACCGTCAAGGCTGAGAAC
ALP	CCACGAAGGGGAACTTGTC	ATGGGATGGGTGTCTCCACA
Runx2	TGCTAATGCTTCGTGTTTCCA	TCCACACCATTAGGGACCATC
OCN	GATGTGGTCAGCCAACTCG	TCACACTCCTCGCCCTATT
OPN	CACACTATCACCTCGGCCAT	TCCTAGCCCCACAGACCCTT

general anesthesia and sterilizing the rats, a complete incision with a depth of 4 mm was made on the proximal medial aspect of the maxillary first molars (M1) DL. The flap was then raised to fully expose the proximal medial side of M1 and the palatine alveolar bone. Using a dental drill, a portion of the alveolar bone was removed at the root bifurcation on the M1 side while ensuring that there was no penetration into the maxillary sinus. Careful measurements were taken with periodontal probes, resulting in the creation of a specific acute periodontal defect measuring 3x2x1 mm^3. This approach exposed the near palatal root surface and adjacent root bifurcation zones. The root surface was then cleaned with a periodontal Gracey scraper to remove any remaining periodontal ligament (PDL) or fragments of alveolar bone. After rinsing with sterile saline, hemostasis was achieved by placing a sterile cotton ball on the defect site. Depending on the experimental design, the appropriate material was inserted into the defect area. Alternatively, the flap was repositioned and secured with a single intermittent suture to achieve primary closure, as shown in Figure 7a. After the surgery, the rats received subcutaneous antibiotic injections every other day for one week. Finally, at 8 weeks post-surgery, the rats were humanely euthanized, and the complete maxilla was meticulously extracted. Each sample was thoroughly washed with distilled water before being promptly immersed in a 4% paraformaldehyde solution.

Micro-CT Analysis

To quantitatively evaluate the impact of different biomaterials on the remodeling of alveolar bone, we utilized a micro-CT scanner (SCANCO Medical AG, Switzerland) to scan specimens 8 weeks after the surgery. The scanner was set to 70 kVp, 83 μA, and 6 W intensity. Multiple scan slices were then rearranged using DataViewer (version 1.5.1.2) and 3D coronal images were reconstructed using CTAn (version 1.13) to analyze new bone formation in the defective area. We used a slice-based approach to determine the volume of interest (VOI). This involved starting at the root furcation and extending 50 layers towards the root. The buccal boundary was identified by connecting the mesial root to the palatal surface of the mesial palatal root, while the mesial boundary was set as the mesial surface of the mesial root. The distal boundary was determined by the distal surface of the mesial root-mesial palatal root, and the palatal boundary was defined as having a specific thickness of 0.35 mm from the buccal side, as indicated by Hounsfield Unit (HU) gray levels. Additionally, we calculated the bone volume to tissue volume (BV/TV), trabecular thickness (Tb.Th), and the ratio of trabecular separation (Tb.Sp).

Histological Analysis

After undergoing radiographic examination, the maxillary specimens were subjected to a three-month decalcification process. Then, they were treated with an upgraded alcohol series dehydrator. The processed tissue was embedded in paraffin wax and sliced into sections, each measuring 4 μm in thickness, using a microtome (RM2265, Leica, Germany). The extent of periodontal defects and regenerative outcomes, including new alveolar bone formation and fiber insertion around the root area, were observed through Hematoxylin-eosin (HE) staining and Masson trichrome staining. Photomicrographs were taken using a vertical microscope (DM4000, Leica, Germany). Samples from each group were

taken at 8 weeks and three close-up perspectives of sections stained with HE and Masson's trichrome within the surgical region were randomly selected. The angle of the fiber bundle to the root surface was measured using the ImageJ software.

Statistical Analysis

The results were presented as the mean and standard deviation (SD) and were analyzed using *t*-tests and one-way ANOVA in GraphPad Prism software (Version 6, MacKiev Software, Boston, MA, USA). A threshold of $P < 0.05$ was used to determine statistical significance.

Results

Characterization of ACP Nanoparticles

After freeze-drying the samples, FTIR was used to identify the chemical composition of ACP. Figure 1a displays the infrared spectra and characteristic peaks of both ACP and ACP/PEG. The distinctive peak of ACP is the PO_4^{3-} vibration peak at 590–610 cm^{-1} and 1000 cm^{-1}.[42] The characteristic peak of PEG is the broad stretching peak of CH_2 at 2886 cm^{-1}, and the prominent stretching vibration peak of C-O at 842 cm^{-1}.[43] XRD, shown in Figure 1b, displayed a broad "bun peak" at 30°, which is characteristic of amorphous calcium phosphate.[44] Figure 1c shows minor changes in the peak map from the first week to the fourth week, suggesting that degradation and remineralization are occurring without noticeable peak splitting, indicating that crystallization is not significant. As seen in Figure 1d, the TEM images of ACP drug carriers synthesized without PEG display short rod-like shapes, likely due to the instability of ACP in solution, which then transforms into HA crystals. When PEG is added, ACP is encapsulated in approximately 20 nm concentric nanospheres, limiting atomic movement and inhibiting crystal growth, thus maintaining stability.

Characterization of Electrospun Core-Sheath Nanofiber Membranes

Figure 2a shows the direct presentation of the core/sheath structure of fibers with ACP-loading, as observed using TEM. SEM was also used to examine the microstructure and surface morphology of two types of core-sheath nanofibers: pristine core-sheath nanofiber (P-CNF) and multi-functional core-sheath nanofiber (Lys/ACP-CNF) (Figure 2b). The P-CNF was

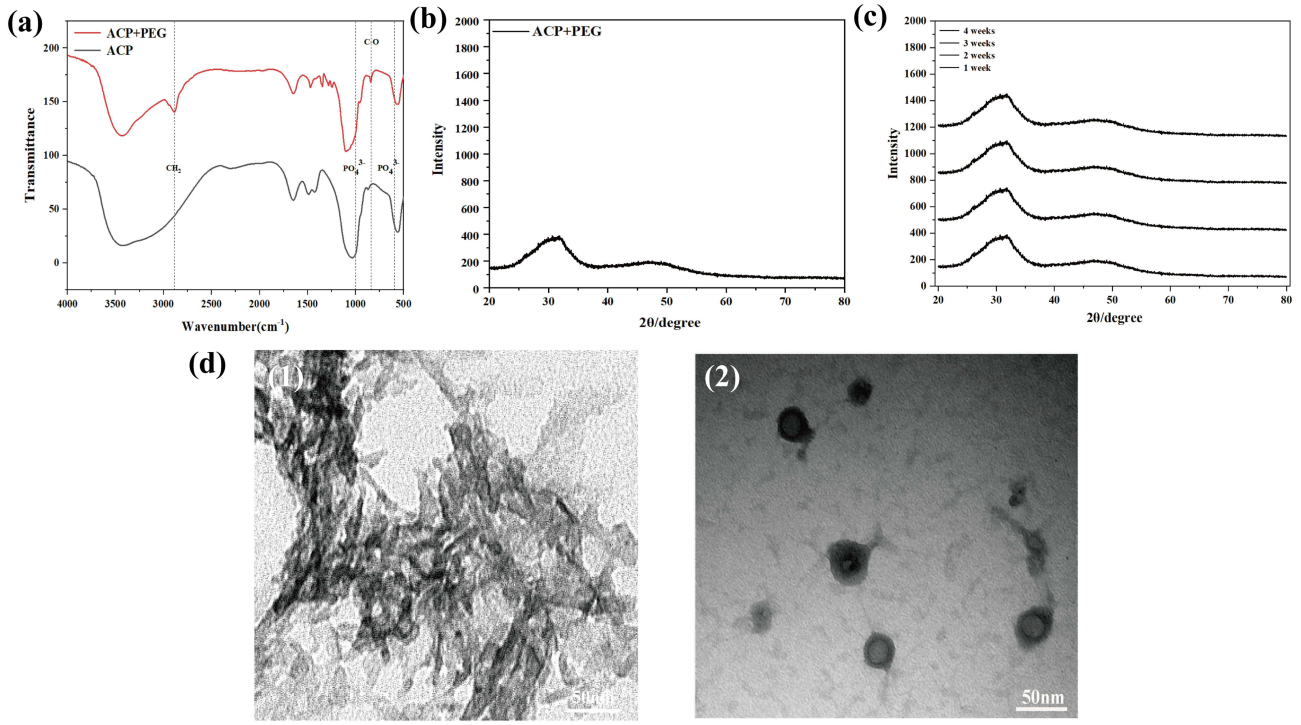

Figure 1 Schematic illustration of the fabrication of the core-sheath nanofiber. Characterization of ACP(**a**) FTIR spectrum of ACP(**b**) X-ray diffraction spectrum of ACP(**c**) X-ray diffraction spectrum of ACP (4 weeks period)(**d**) Transmission electron micrographs of ACPs prepared with (2) or without PEG (1).

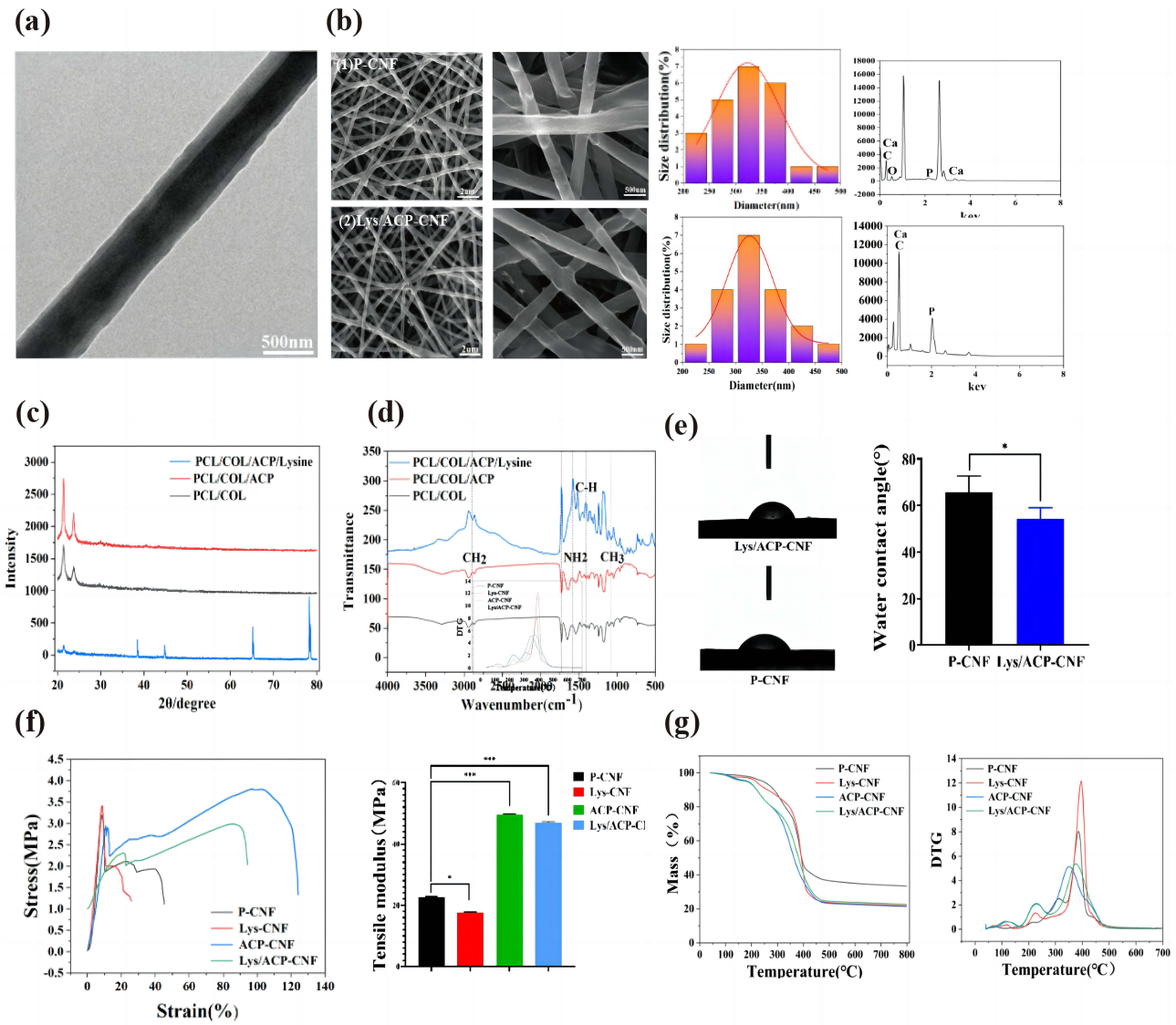

Figure 2 Characterization of core-sheath nanofibers(**a**) Transmission electron microscopy (TEM) of Lys/ACP-CNF(**b**) SEMof core-sheath nanofiber with(1) or without(2) L-Lysine and ACP(**c**) X-ray diffraction spectrum of core-sheath nanofiber (**d**) FTIR spectrum of core-sheath nanofiber(**e**)Water contact angle of core-sheath nanofiber(**f**) Mechanical properties of core-sheath nanofiber (**g**) Thermogravimetric analysis (TGA) of core-sheath nanofiber.
Note:(*: $P < 0.5$; ***: $P < 0.001$).

made of PCL/COL without any drug-loading, while the Lys/ACP-CNF contained L-lysine in the PCL/COL shell and ACP in the PCL/COL core.The diameters of these two types of nanofibers were found to be 322.91±106.46 nm and 146.61±16.62 nm, respectively.There was no significant difference between the two ($P > 0.05$).EDS mapping in Figure 2b confirmed the presence of ACP in the core-sheath nanofiber, with the presence of calcium and phosphorous elements in the Lys/ACP-CNF nanofiber.This confirms that the Lys/ACP-CNF has a clear coaxial structure and a relatively uniform fiber morphology.FTIR was used to identify functional groups in electrospun PCL and COL films, such as OH at 3400–3500 cm^{-1}, NH_2 at 1638 cm^{-1}, and O-C-NH_2.Additionally, CH_3 and CH_2-O were detected in the range of 1000–1200 cm^{-1}. The FTIR spectrum of PCL showed no major modifications in the related functional groups of CH_2 and CH_3 at the range of 2900–3000 cm^{-1} (Figure 2c).XRD analysis of PCL material revealed crystalline diffraction peaks at 21.323° and 23.694°, with a higher intensity in Lys/ACP-CNF compared to P-CNF.This suggests an increased degree of crystallinity after the addition of ACP[45] (Figure 2d).The hydrophilicity of electrospun membranes is a critical factor in the successful adhesion of cells onto core-sheath nanofiber surfaces in tissue engineering.[46] To evaluate this, we measured WCA of Lys/ACP-CNF and P-CNF (Figure 2e).The results showed that the WCA of Lys/ACP-CNF was significantly lower than that of P-CNF (65.65 ±

5.55° vs 54.37 ± 3.37°, P <0.05), indicating that the addition of L-lysine improved the hydrophilicity of Lys /ACP-CNF. As shown in Figure 2f, the fracture strain of electrospun core-sheath nanofibers was found to be more elastic and less strengthened after integrating ACP. This resulted in an increase in the Young's modulus from 22.48 ± 0.06 MPa to 49.53 ± 0.03 MPa (P < 0.05). However, the Young's modulus of the ACP-CNF (49.53 ± 0.03 MPa) was higher than that of the Lys/ACP-CNF group (46.83 ± 0.09 MPa), which can possibly be attributed to a decrease in polymer crystallinity after the addition of L-lysine. This suggests that the fibrous framework became stronger after the addition of ACP, and the tensile strength of the Lys/ACP-CNF group exceeded that of the unloaded group. Thermal analysis of the P-CNF, ACP-CNF, Lys-CNF, and Lys/ACP-CNF samples revealed a two-stage thermal degradation process (as shown in Figure 2g). The first stage, which ranged from 50°C to 230°C, was attributed to the evaporation of moisture. The following stage, starting at around 250°C and ending at 500°C, was the main region for thermal degradation. It has been proposed that enhanced thermal stability can be achieved if the measured Tmax (maximum temperature) of one component increases to the higher Tmax of another component, indicating diverse interactions between the two elements. In the case of Lys/ACP-CNF, the decreased Tmax of L-lysine shifted towards the higher Tmax of ACP, suggesting the presence of interactions between L-lysine and ACP within the composite core-sheath nanofiber(Figure 2g).The findings above confirm that Lys/ACP-CNF demonstrates the necessary mechanical strength of a core-sheath nanofiber to prevent membrane collapse.Additionally, it exhibits appropriate hydrophilicity and thermodynamic characteristics, which are essential prerequisites for a suitable core-sheath nanofiber for biomedical applications.[47]

Cellular Viability and Morphology on Core-Sheath Nanofibers

The results of the EdU labeling assay showed that the proliferation rate of PDLSCs was not significantly affected by the Lys/ACP-CNF group.There was no significant difference in the percentage of EdU-positive cells between the Lys/ACP-CNF group and the control group (Figure 3a). The relationship between PDLSCs and core-sheath nanofiber was examined using CLSM to observe adhesion and morphology of the cells on different substrates. After 3 days of culturing, cells grown on HA maintained their typical long spindle shape, while those on P-CNF and Lys/ACP-CNF had slender actin filaments and increased spreading pseudopodia (Figure 3b).The Live/Dead assay showed no

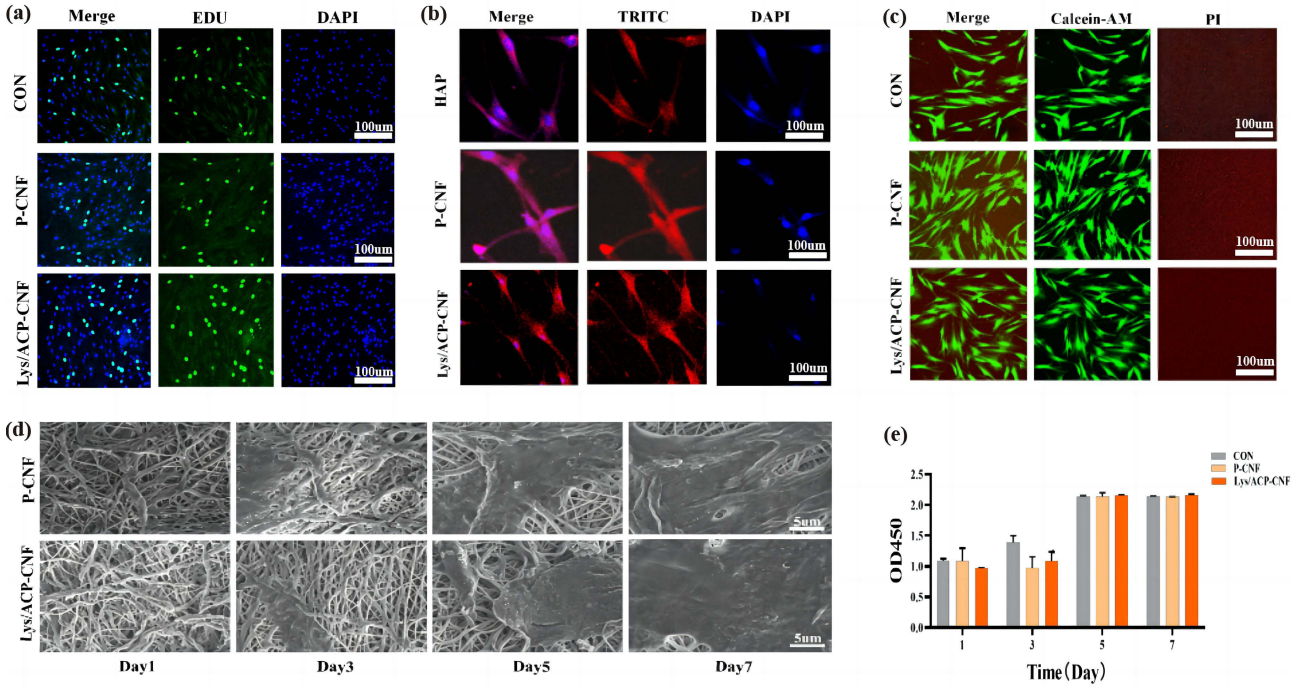

Figure 3 (**a**) EdU labeling assay (**b**) Nuclear (blue) and cytoskeleton (red) staining of PDLSCs cultured on core-sheath nanofibers for 3 days (**c**) Live/dead staining of core-sheath nanofiber(**d**) SEM images of PDLSCs cultured on core-sheath nanofibers for 1, 3, 5, and 7 days (**e**)CCK-8 assay.

cytotoxicity from contact. After 72 hours, a large number of viable green cells were observed on all core-sheath nanofibers, with only a few dead red cells. These cells were evenly distributed and formed many cell-cell contacts (Figure 3c). The cells were observed via SEM on the first day and were seen extending pseudopods. They adhered to and interwove with the fibers, as shown in Figure 3d. On the third and fifth days, the PDLSCs displayed elongated cytoskeletons and took on spindle-like or polygonal shapes. By the seventh day, it was evident that the PDLSCs had completely covered the membrane's surface. To examine the impact of core-sheath nanofiber on cell vitality, PDLSCs were used and the results of the CCK-8 assay showed no significant difference between the control group and the P-CNF group from day 1 to day 3. This indicates that the core-sheath nanofiber had favorable biocompatibility with PDLSCs. However, the Lys/ACP-CNF group showed a noticeable inhibitory effect on the early-stage growth of PDLSCs, which could be attributed to the initial burst release of L-lysine. From day 5 to day 7, there was no significant difference in growth between the Lys/ACP-CNF group and the control group, as shown in Figure 3e.

The compatibility of nanomaterials with cells is a necessary aspect for their potential use in a biological context.[48] The earlier mentioned study revealed the in vitro biological effects of Lys/ACP-CNF on crucial cells involved in the regeneration process of periodontal tissue.[49]

The Controlled Release Assay

Figure 4a shows the 20-day cumulative release profiles of L-lysine from Lys/ACP-CNF core-sheath nanofibers. The release pattern is biphasic, with two distinct phases: an initial burst release on the first day (stage I) and a sustained release (stage II). During the initial stage, approximately 6% of L-lysine was released. This could be due to the quick detachment of surface-distributed L-lysine on the nanofibers, resulting in a burst release. Figure 4b depicts a gradual decrease over time in the relative content of calcium and phosphate ions in Lys/ACP-CNF, providing evidence of the release of ACP nanoparticles from Lys/ACP-CNF.

In vitro Antibacterial Activity

The effectiveness of the Lys/ACP-CNF group in suppressing the formation of single and dual-species biofilms by *F.n* was evaluated using CV staining. The results showed that after 24 hours of incubation, the Lys/ACP-CNF group was able to decrease the formation of *F.n* biofilms from 0.21 ± 0.0073 to 0.09 ± 0.0064.This trend continued at 36 and 48 hours (Figure 5a). In contrast, without Lys/ACP-CNF, the *F.n* biofilm was consistently distributed and covered the cell surface. However, with the addition of Lys/ACP-CNF, the biofilm appeared to be looser and formed smaller clusters. Similarly, the Lys/ACP-CNF group showed inhibitory effects on dual-species biofilms with *F.n* and *P. g* (Figure 6a). SEM

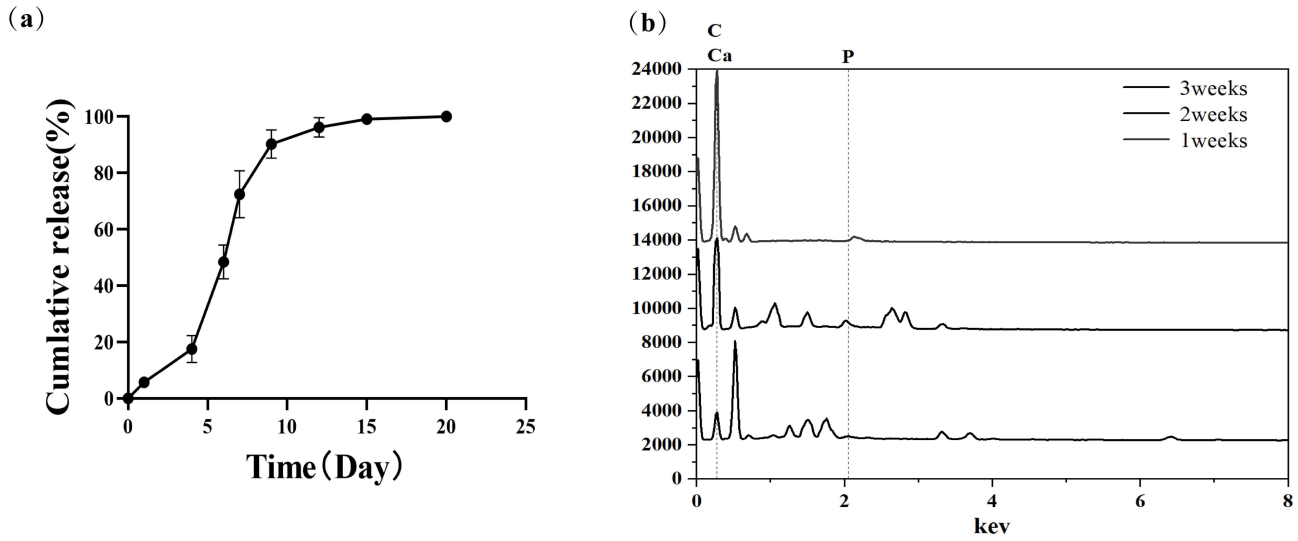

Figure 4 (**a**) The release profiles of L-lysine from lys/ACP-CNF for 20 days(**b**) The release profiles of calcium and phosphate ions from lys/ACP-CNF for 20 days.

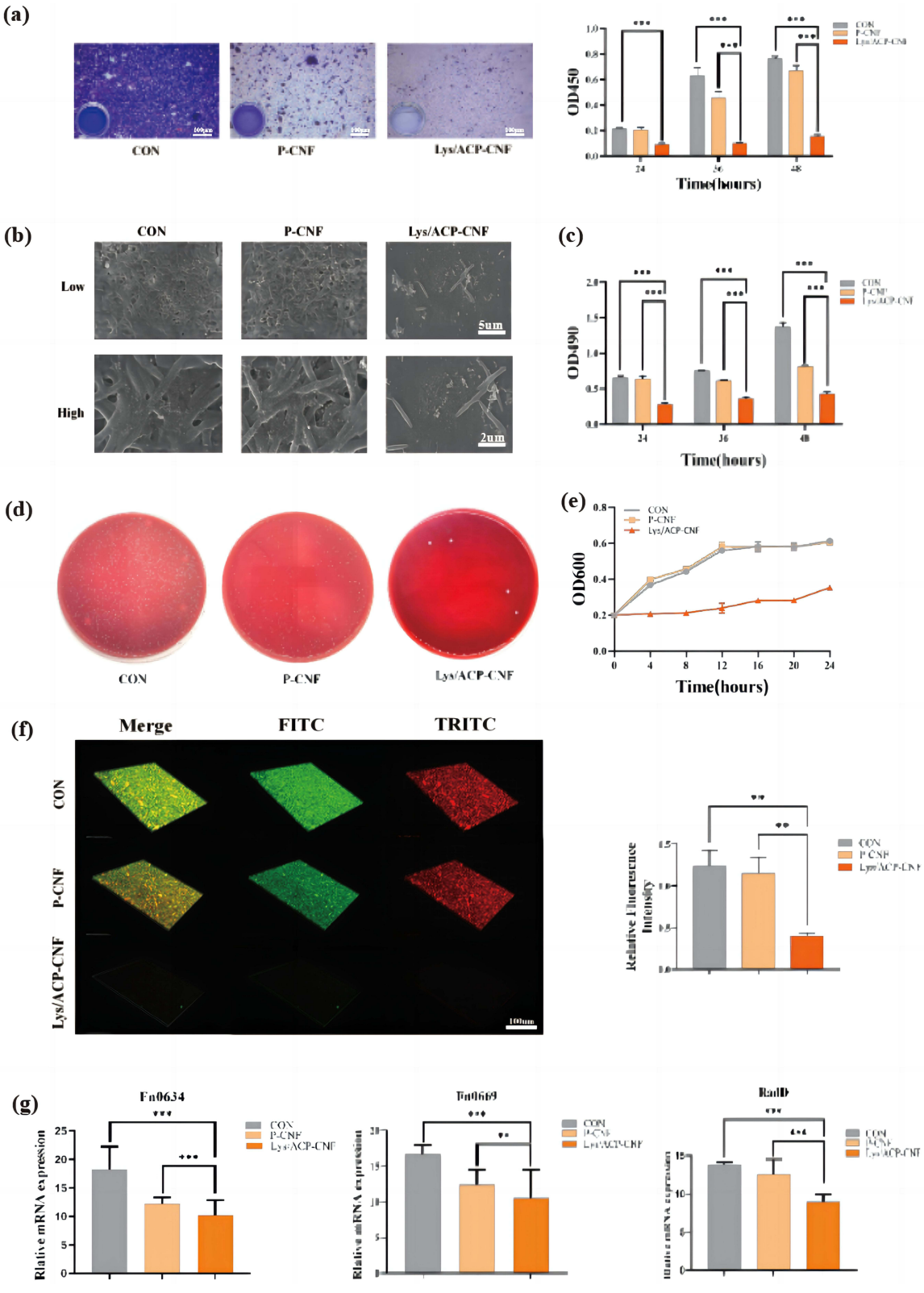

Figure 5 (**a**) The crystal violet staining photograph of *F. nucleatum* biofilm cultured with Lys/ACP-CNF (**b**) The SEM photograph of *F. nucleatum* biofilm cultured with Lys/ACP-CNF (**c**) The EPS quantitative analysis of *F. nucleatum* biofilm cultured with Lys/ACP-CNF (**d**) The image of *F. nucleatum* bacterial colony treated with Lys/ACP-CNF(**e**) Bacterial killing kinetic curves of *F. nucleatum* cultured with Lys/ACP-CNF (**f**) The structure of biofilms of *F. nucleatum* cultured with Lys/ACP-CNF as observed via CLSM. (**g**) The mRNA expression of Fn0634, Fn0669 and RadD in *F. nucleatum* cultured with Lys/ACP-CNF.
Note: (**: $P < 0.01$; ***: $P < 0.001$).

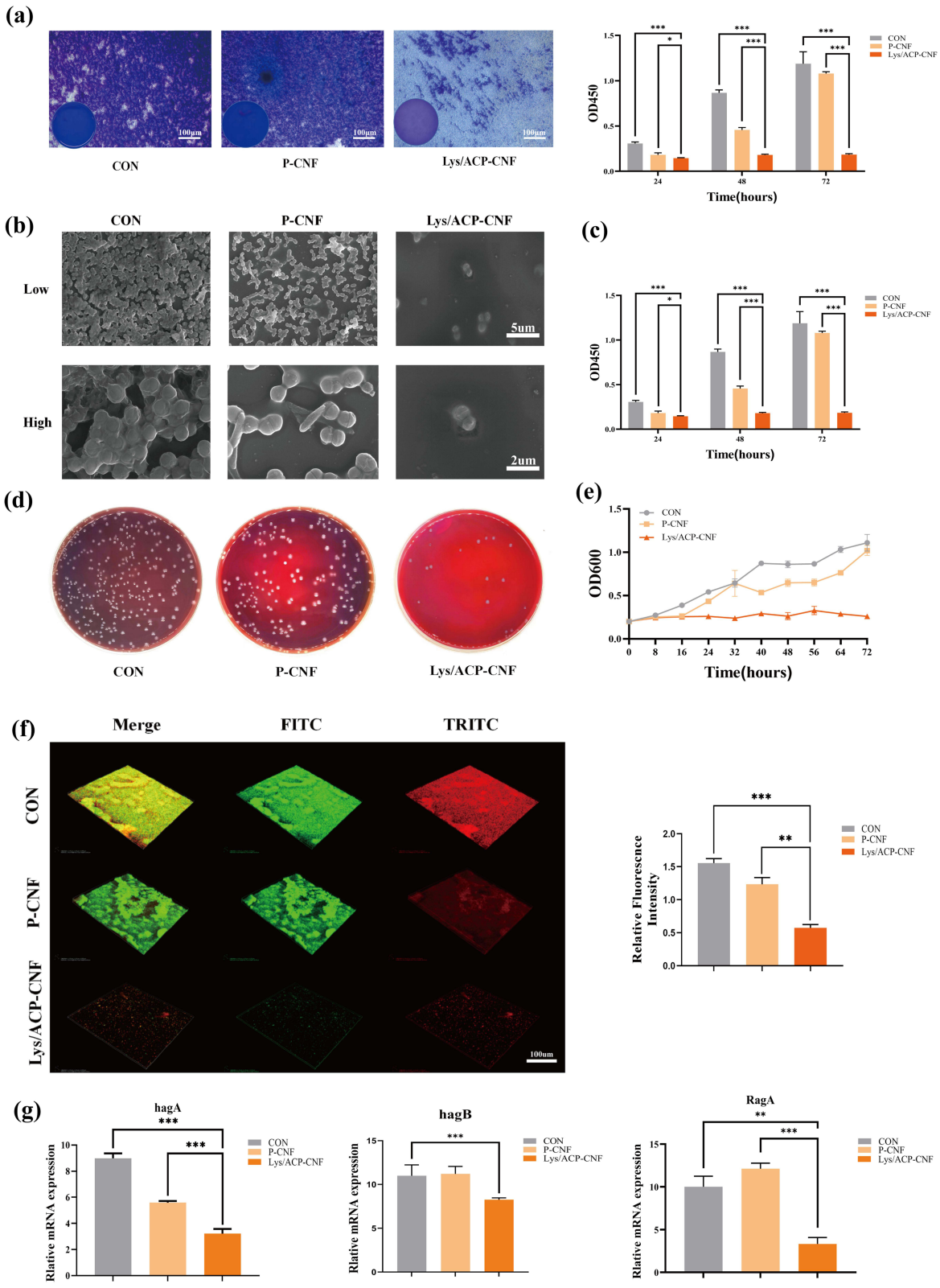

Figure 6 (**a**) The crystal violet staining photograph of *F. nucleatum* and *P. gingivalis* biofilm cultured with Lys/ACP-CNF (**b**) The SEM photograph of *F. nucleatum* and *P. gingivalis* biofilm cultured with Lys/ACP-CNF (**c**) The EPS quantitative analysis of *F. nucleatum* and *P. gingivalis* biofilm cultured with Lys/ACP-CNF (**d**) The image of *F. nucleatum* and *P. gingivalis* bacterial colony treated with Lys/ACP-CNF (**e**) Bacterial killing kinetic curves of *F. nucleatum* and *P. gingivalis* cultured with Lys/ACP-CNF (**f**) The structure of biofilms of *F. nucleatum* and *P. gingivalis* cultured with Lys/ACP-CNF as observed via CLSM (**g**)The mRNA expression of hagA, hagB and RagA in *F. nucleatum* and *P. gingivalis* cultured with Lys/ACP-CNF.

Note: (*: $P < 0.5$; **: $P < 0.01$; ***: $P < 0.001$).

examination revealed that *F.n* formed a compact, three-dimensional biofilm composed of spindle-shaped rods with intact cell membranes and layers of bacteria. The Lys/ACP-CNF group significantly reduced the number of *F.n* cells and disrupted the structure of the biofilm (Figure 5b). In the *F.n* and *P.g* dual-species biofilm, there was also a decrease in *P.g*, although not as significant as in the case of *F.n*. It can be observed that the Lys/ACP-CNF group no longer contains spindle-shaped rods. However, the round-shaped *P.g* can still be found (Figure 6b).

In mature biofilms, the EPS matrix is composed of various polymeric substrates, that are crucial in forming a three-dimensional biofilm architectural scaffold. The main component of the EPS matrix is the exopolysaccharide, which plays a fundamental role in promoting adhesion and maintaining structural integrity allowing for the formation of bacterial aggregates.[50] The incorporation of Lys/ACP-CNF into single-species biofilms of *F.n* and dual-species biofilms of *F.n*/*P.g* caused a significant decrease in EPS production after 24, 36, and 48 hours of incubation (Figure 5c and 6c). The EPS production in *F. n* mono-species biofilm decreased from 0.65 ± 0.033 to 0.28 ± 0.031 at 24 hours and was further reduced from 1.36 ± 0.083 to 0.42 ± 0.035 at 48 hours. The EPS production in *F.n* and *P.g* dual-species biofilm decreased from 0. 4779± 0.013 to 0. 22± 0.022 at 24 hours and was further reduced from 1.42 ±0.096 to 0.27 ±0.064 at 72 hours.The antibacterial efficacy of the Lys/ACP-CNF group was determined by a plate counting assay, which showed a significant decrease in the number of bacterial colonies of *F.n* in the Lys/ACP-CNF group (Figure 5d), indicating the antibacterial activity of the core-sheath nanofiber. Additionally, the presence of Lys/ACP-CNF significantly hindered the growth of both *F.n* and *P.g*.Compared to P-CNF,Lys/ACP-CNF displayed a significant decrease in the number of bacterial colonies after 24 h inoculation. (Figure 6d).

The results of the study on bacterial growth showed that the Lys/ACP-CNF group had an antibacterial effect on *F.n*. This was evidenced by the inhibition of bacterial growth in comparison to the control group. Additionally, the growth of both *F. n* and *P.g* were inhibited in response to treatment with the Lys/ACP-CNF group. However, treatment with P-CNF did not show any significant differences when compared to the control group (Figure 5e and 6e). Further results from CLSM showed that the Lys/ACP-CNF group caused a significant decrease in the number of *F.n* bacteria, as well as disruption of the biofilm structure (Figure 5f). Treatment with Lys/ACP-CNF also resulted in a notable reduction in biofilm thickness, as seen through staining with SYTO 9 and PI on dual-species biofilms of *F.n* and *P.g*. The biofilms formed by *F.n* and *P.g* were consistently distributed and fully covered the surface where the bacteria were attached without Lys/ACP-CNF. However, the addition of Lys/ACP-CNF caused the biofilms to become looser and form smaller clusters. These results demonstrated that the presence of Lys/ACP-CNF suppressed the production of exopolymeric substrates by bacterial cells in biofilms. This discovery is consistent with the findings obtained from the EPS assay.(Figure 6f).

To gain insights into gene expression, we used RT-qPCR analysis to measure the impact of Lys/ACP-CNF on the formation of biofilms by *F.n* and *P.g*. The selected genes included FN0669, which codes for the ATP binding protein znuC of the High-affinity zinc uptake system, FN0634 encoding the GTP binding protein TypA/BipA, and FN1162 (RadD) encoding the enzyme hydroxyacylglutathione hydrolase. Additionally, the analysis included virulence factor genes of *P.g*, such as hagA, hagB, and RagA, which are known for their involvement in adhesion, invasion, and host colonization.[51] Lys/ACP-CNF seemed to decrease the expression of all six genes tested in biofilms (Figure 5g and 6g).

In this section, it was determined that Lys/ACP-CNF has the ability to inhibit the formation of *F. n* biofilm in vitro. Additionally, CLSM was used to observe the disruption of the three-dimensional structure of the *F.n* biofilm. The impact of Lys/ACP-CNF L-lysine on the adhesion factor RadD and virulence factors was also identified through RT-qPCR.[51] *P. g* is the primary pathogenic bacterium in periodontitis.[52] We have discovered that Lys/ACP-CNF has the ability to inhibit biofilm formation by *F.n* and *P.g*, showing potential for promoting the regeneration of alveolar bone.

In vitro Osteogenesis Study

We further clarified the osteogenic differentiation of Lys/ACP-CNF by measuring the gene expression levels of ALP, Runx2, OPN, and OCN on three substrates using RT-qPCR. ALP and Runx2 serve as markers for the initial stages of osteoblastic cell differentiation, while OPN and OCN play significant roles in the bone matrix mineralization process.As shown in Figure 7a, Lys/ACP-CNF has displayed potential in stimulating the osteogenic differentiation of PDLSCs[53,54] (Figure 7a). Figure 7b illustrates the absorbance of ARS from the stained calcium deposits on the core-sheath nanofibers. It reveals that the Lys/ACP-CNF group not only showed a stronger ARS staining at 7 and 14 days compared to the

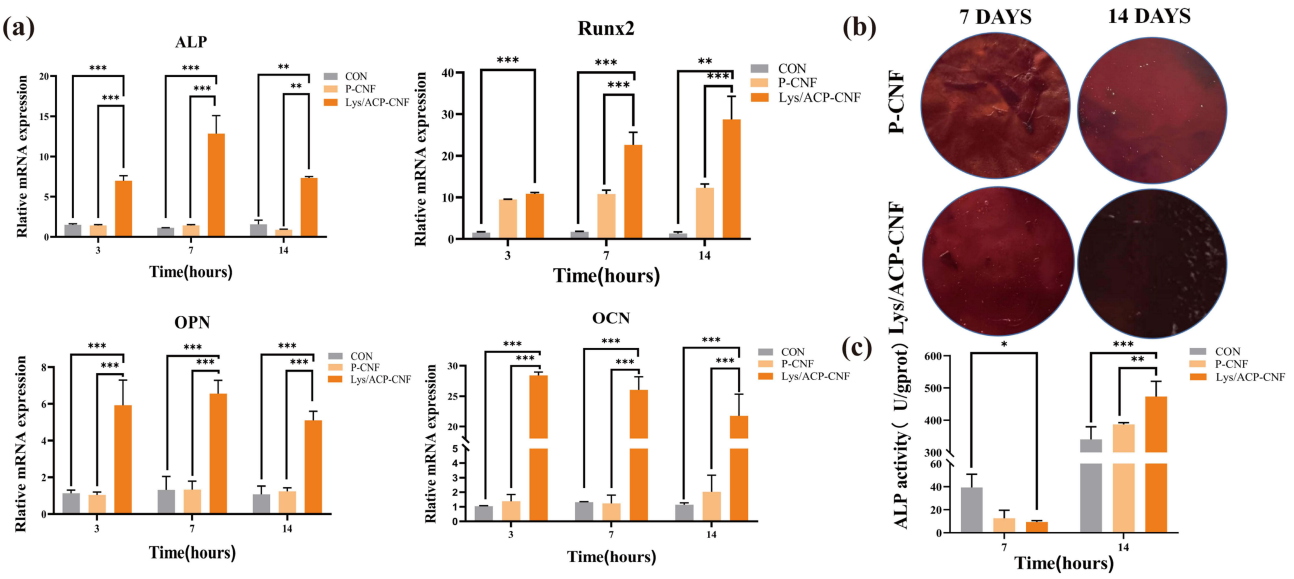

Figure 7 (**a**) The mRNA expression of ALP, Runx2, OPN and OCN in PDLSCs cultured with Lys/ACP-CNF (**b**) Alizarin red S (ARS) assay (**c**) The quantitative analysis of ALP on day 7 and day14.
Note:(*: $P < 0.5$; **: $P < 0.01$; ***: $P < 0.001$).

P-CNF group, but it also outperformed it in terms of the extracted ARS optical density at 562 nm. These findings confirm the biomineralization capabilities of the composite core-sheath nanofibers.

The ALP activity, which is an early and crucial marker for stem cell differentiation into osteogenic tissue, was measured. Figure 6c shows the protein activity of ALP in PDLSCs cultured on three different substrates. There was no significant difference in ALP activity between the Lys/ACP-CNF group and the control and P-CNF groups on day 7 ($P < 0.001$).However, on day 14, there was a notable increase in ALP activity for all three substrates. As expected, the cells cultured on Lys/ACP-CNF showed the highest ALP activity ($P < 0.001$) (Figure 7c). These findings suggest that Lys/ACP-CNF has the potential as a beneficial core-sheath nanofiber for bone tissue engineering.

In vivo Evaluation of Alveolar Bone Regeneration

As mentioned before, rats models were conducted to examine the effects of Lys/ACP-CNF on anti-periodontitis in vivo (Figure 8a). The experimental groups were labeled as follows: 1.Healthy, 2.Defect, 3. Defect $+10^8$ *F. nucleatum* injection for 3 days (Defect+*Fn*), 4. Defect $+10^8$ *F. nucleatum* injection for 3 days + Lys-CNF (Defect+*Fn*+Lys-CNF), 5. Defect $+10^8$ *F. nucleatum* injection for 3 days + Lys/ACP-CNF (Defect+*Fn*+Lys/ACP-CNF). We utilized Micro-computed tomography (Micro-CT) to analyze the in vivo regeneration of alveolar bone. We employed CT Vox and DataViewer software to construct three-dimensional digital and cross-sectional images of the alveolar bone, as shown in Figure 8b. Compared to the control group, the Defect+*Fn* group exhibited significant reconstruction of alveolar bone defect after 8 weeks. In contrast, the addition of Lys/ACP-CNF to the defect site demonstrated alveolar bone reconstruction with new bone formation in the root bifurcation region. CTAn software was used to calculate BV/TV around the first molar. The results shown in Figure 8c indicated that rats in the Defect+*Fn*+Lys-CNF group had the highest BV/TV ratio. This result was consistent with the in vitro antibacterial results, confirming the effectiveness of Lys/ACP-CNF in preventing infection during alveolar bone reconstruction.The quantitative analysis also revealed that the Defect+*Fn*+Lys/ACP-CNF group had the highest Tb. N and the lowest Tb. Sp among all groups. These parameters were similar to those observed in healthy periodontal bone tissue.

After being scanned using micro-CT, the rats' maxillary bones were examined using histopathological methods. The micrographs of HE and Masson trichrome stained tissue sections are shown in Figure 8d. Rats in both the Defect and Defect+*Fn* groups showed varying degrees of inflammatory response (including incomplete epithelium, epithelial hyperplasia, irregular basal cell arrangement, and inflammatory cell infiltration). Treatment with Lys/ACP-CNF reduced

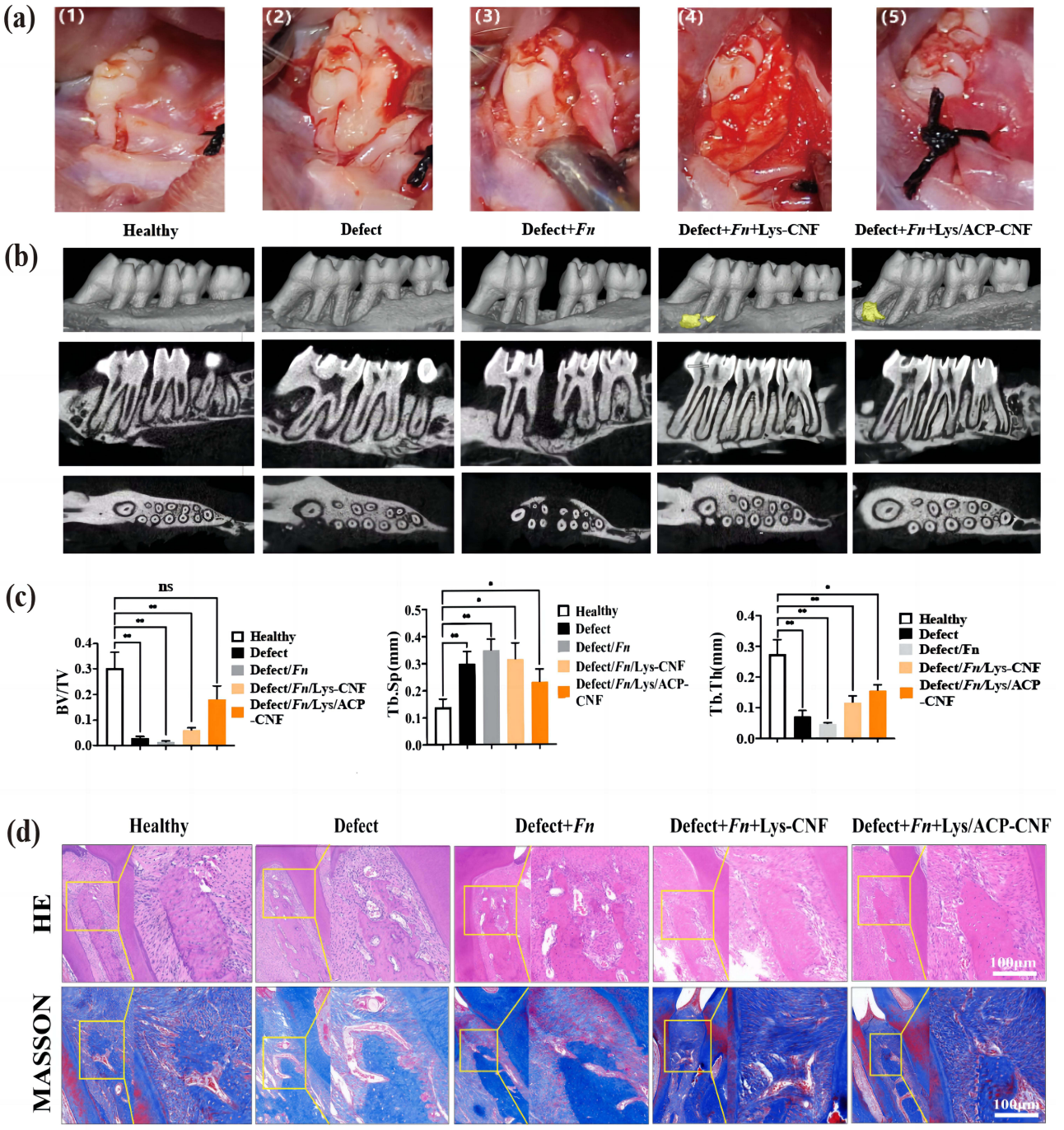

Figure 8 (**a**) The modeling process in rats(**b**) The three-dimensional micro-CT images of alveolar bone in the healthy rats, periodontitis rats and the rats treated with Lys/ACP-CNF(**c**) BV/TV,Tb.sp,Tb.Th.calculate from micro-CT results(**d**)The Histological and immunohistochemical analysis of the rat periodontal tissue regeneration.
Note:(*: $P < 0.5$; **: $P < 0.01$).

the inflammatory responses. This was shown by normal epithelial cell morphology, tight arrangement, and the absence of obvious inflammatory changes in the lamina propria (Figure 8d). Ultimately, random rats were selected from each group, and histological analyses of vital organs such as the heart, liver, spleen, lungs, and kidneys were conducted over an 8-week period. No discernible variations were observed among the different rat groups, indicating the potential non-toxicity of Lys/ACP-CNF (Figure 9).

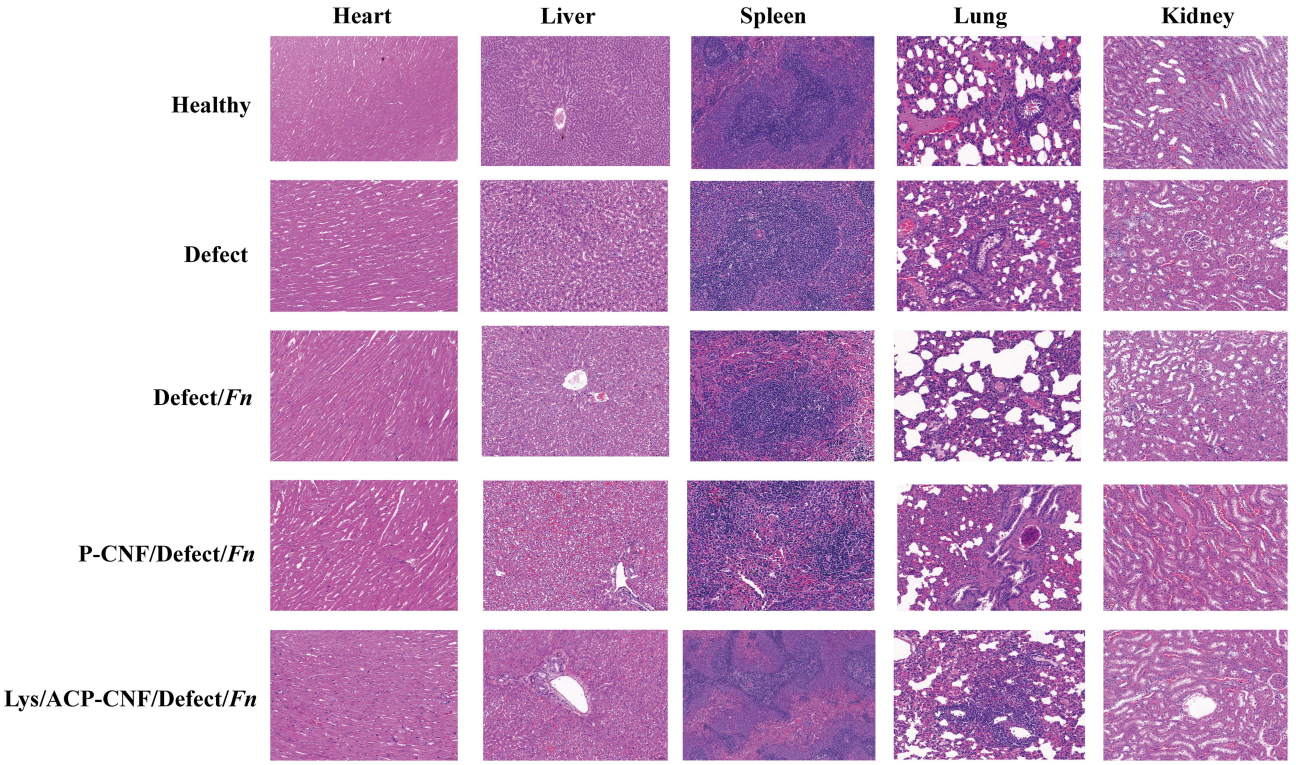

Figure 9 The Histological staining of major organs (heart, liver, spleen, lung, and kidney) in different group of rat for 8 weeks.

Discussion

The complex nature of periodontal tissue makes regeneration therapy a significant challenge. The process involves separate but overlapping stages for regenerating different compartments. For successful tissue engineering of the periodontium, the ideal drug-loading GTR membrane must possess specific properties such as osteoinductivity, antibacterial function et.al[55,56] Currently, the most commonly used methods in clinical mainly aim to prevent postoperative epithelial cells from migrating to the wound surface, providing an opportunity for specific cell populations residing in the periodontal tissue to fill periodontal injuries or defects and reverse periodontal destruction.[57] However, their role in the formation of bacterial biofilms, which are the primary cause of periodontitis, is limited. Therefore, it is crucial to use an appropriate membrane that can control the release of different drugs in specific locations to induce desired functions. In our experiment, a new core-sheath nanofiber membrane with excellent comprehensive performance by adding amorphous calcium phosphate (ACP) and L-lysine in the process of coaxial electrospinning was successfully synthesized.

In this study, we analyzed the characterization of core-sheath nanofiber membranes by various suitable research methods. The TEM results showed that the Lys/ACP-CNF demonstrated a clear coaxial structure and relatively uniform fiber diameter. The mechanical strength of the nanofiber membrane is a crucial factor in preventing the collapse of the membrane, and appropriate hydrophilicity and thermodynamic properties are necessary for the biocompatibility of nanofiber membrane as well as their biological functions. The tensile strength and Young's modulus of the Lys/ACP-CNF were significantly increased compared with those of the Lys-CNF group, suggesting that the incorporation of ACP effectively improved the mechanical strength of the membrane. The water contact angle test showed that the addition of L-lysine can improve the hydrophilicity of the membrane, although L-lysine destabilizes Lys/ACP-CNF's thermally. However, ACP can counteract this disadvantage. The study also examined the biological activity of PDLSCs in vitro to investigate whether Lys/ACP-CNF has biological effects on key cells involved in periodontal tissue regeneration. As shown in Figure 3, Lys/ACP-CNF promoted the adhesion ability of PDLSCs without adversely affecting cell activity. This could be due to the hydrophilic surface that facilitates the absorption of fibronectin, resulting in highly attached cells.[49] In the Lys/ACP-CNF release system, L-lysine was released at a faster rate during the early stage and calcium and

phosphate ions from ACP maintained a slow and stable release rate over three weeks. Our study showed that the initial burst release of L-lysine has a strong inhibitory effect on the biofilms formation by *F.n* and *P.g*. Moreover, the release of calcium and phosphate ions from ACP also promotes osteogenesis (Figure 4).

In the process of treating alveolar bone defects caused by periodontitis, relying solely on the effect of Lys/ACP-CNF on PDLSC adhesion is not sufficient.[58] If Lys/ACP-CNF can also inhibit the formation of pathogenic bacterial biofilms, it can aid in the functional regeneration of alveolar bone. Therefore, the study further investigated the potential of Lys/ACP-CNF to inhibit biofilm formation by *F.n* and *P.g*. Our previous research has shown that lysine can inhibit the formation of *F.n* biofilms in vitro.[15] In this experiment, we used plate counting assay, antibacterial curve, EPS experiment, etc. to explore the effect of Lys/ACP-CNF on the formation of *F.n* mono-specie biofilms and *F.n* and *P. g* dual-species biofilms. As shown in Figure 5, for *F. n* mono-specie, Lys/ACP-CNF can significantly affect the formation of biofilms. In SEM experiments, bacteria dispersed from continuous and tightly packed biofilms into individual, short rod-shaped bacteria. This shows that Lys/ACP-CNF has superior biofilm-dispersion and antibactericidal effects. The experiments of crystal violet and EPS also showed significant anti-biofilm effects. In addition, we observed the destruction of the *F.n* mono-species biofilm structure, changing from a three-dimensional configuration to a flattened structure through CLSM. In the final part of this section, we also discovered the effect of Lys/ACP-CNF on the adhesion factor RadD and virulence factors through RT-qPCR.[51]

We also studied the effect of Lys/ACP-CNF on *F.n* and *P.g* in a dual-species biofilm because *P.g* is the main pathogenic bacterium of periodontitis.[52] Although the effect of Lys/ACP-CNF on the formation of dual-species biofilms of *F.n* and *P.g* was not as significant as that of a mono-specie of *F.n*, it still shows promise for future application. However, the scope of this experiment is currently limited. We will continue to further investigate its potential impact on other strains such as *Staphylococcus* in the future.

Additionally, we evaluated the osteogenic potential of Lys/ACP-CNF in vitro by using periodontal stem cells with multidirectional differentiation potential.[59] The osteogenic differentiation of PDLSCs was consistently reported, as well as their superior tendon differentiation potency.[55] Our RT-qPCR analysis showed an increased trend in the expression levels of OPN and OCN in PDLSCs when compared to the control group. Furthermore, ALP and ARS assays, revealed that in the Lys/ACP-CNF group, PDLSCs exhibited significantly higher levels than both the control and P-CNF groups. These results suggest that Lys/ACP-CNF has potential as a core-sheath nanofiber for bone tissue engineering, promoting the osteogenic differentiation of stem cells.

To further understand the effectiveness of Lys/ACP-CNF, we conducted in vivo experiments on a rat model with periodontal deficiency and implanted electrospun membranes. The membranes were cut into 3*2*1 mm rectangles and placed in the defect region and cover the exposed root surface. We chose the con, Lys-CNF, and Lys/ACP-CNF groups to demonstrate the promotional effect of ACP on osteogenesis in vivo. Micro-CT analysis showed that Lys/ACP-CNF has a high degree of *ro* osteogenic induction and potential for new bone regeneration, which is consistent with cellular research. Additionally, it has the ability to remove biofilms. HE staining showed an improvement in the inflammatory response with normal epithelial cell morphology and tightly arranged cells and no discernible inflammatory changes in the intrinsic layer. In conclusion, through Micro-CT and HE staining, we have demonstrated the regenerative capabilities of Lys/ACP-CNF in periodontal defect regions.

Conclusion

We have developed novel core-sheath nanofibrous membranes with core/shell fiber structures that are loaded with ACP and L-lysine. Morphological observation by SEM and TEM confirms the core-shell structure of the nanofibers. These core-sheath nanofibers have also shown good biocompatibility in vitro, antagonizing *F.n* and *P.g* biofilms, as well as promoting PDLSCs differentiation into osteoblasts. Our subsequent experiments have substantiated the regeneration of periodontal structures, facilitated by the utilization of Lys/ACP-CNF. As a result, this dual-molecule, sustained-release core-sheath nanofiber could potentially rectify alveolar bone loss induced by chronic periodontitis. This development could herald the advent of more efficacious and appropriate materials for periodontal regeneration.

Abbreviations

CNF, core-sheath nanofiber; Lys, L-lysine; GTR, Guided Tissue Regeneration; ACP, amorphous calcium phosphate; TCP, tricalcium phosphate; HA, hydroxyapatite; PDLSCs, periodontal ligament stem cells; *Fn, F.nucleatum; Pg, P.gingivalis*; PCL, Poly(ε-caprolactone); COL, TypeI collagen; PEG, Polyethylene Glycol; FTIR, Fourier Transform Infrared Spectrometer; XRD, X-ray diffraction; TEM, Transmission electron microscopy; HFLP, Hexafluoroisopropanol; PBS, phosphate-buffered saline; UV, Ultraviolet; SEM, Scanning electron microscope; TGA, Thermogravimetric analysis; CLSM, confocal laser scanning microscopy; BHI, brain-heart infusion; EPS, extracellular polysaccharide; CFU/mL, colony-forming units per milliliter; ARS, Alizarin Red S;ALP, Alkaline phosphatase; RT-qpcr, Reverse transcription quantitative polymerase chain reaction; SD rat, Sprague-Dawley rHFLPat; M1, the maxillary first molars; PDL, periodontal ligament; VOI, volume of interest; HU, Hounsfield Unit; BV/TV, the bone volume to tissue volume; Tb.Th, trabecular thickness; Tb. Sp, the ratio of trabecular separation; HE, Hematoxylin-eosin; WCA, water contact angle; OCN, osteocalcin; OPN, osteopontin; Runx2, runt related transcription factor 2; ALP, alkaline phosphatase; hagA, hemagglutinin A; hagB, hemagglutinin B; RagA, Ras-related GTP-binding protein.

Data Sharing Statement

The data, analytical methods and study materials that support the findings of this study can be made available on request to the corresponding authors who manage the information.

Ethics Approval and Consent to Participate

The experiments were approved by the Ethics Committee and the Animal Care and Use Committee of Nanjing Agricultural University (Approval Code: PZW2023039).

Acknowledgment

The authors expressed their gratitude to Xinyue Wang for providing grammar checking.

Author Contributions

Each author played a crucial role in the reported work, contributing to its conception, study design, execution, data acquisition, analysis, and interpretation. Additionally, they actively participated in drafting, revising, and critically reviewing the article. All authors provided final approval for the published version, reached consensus on the submitting journal, and collectively agree to be accountable for every aspect of the work.

Funding

This work was supported by National Natural Science Foundation of China under Grant/Award Number 51972167, Postdoctoral research Foundation of Nanjing(2023) and Key projects of social development of Jiangsu Department of Science and Technology under Grant/Award Number BJ21006. The sponsors had no involvement in any of the stages from study design to submission of the paper for publication.

Disclosure

The authors declare no conflicts of interest in this work.

References

1. Albandar JM, Kingman A. Gingival recession, gingival bleeding, and dental calculus in adults 30 years of age and older in the United States, 1988-1994. *J Periodontol*. 1999;70(1):30–43. doi:10.1902/jop.1999.70.1.30
2. Hatz CR, Cremona M, Liu CC, Schmidlin PR, Conen A. Antibiotic prophylaxis with amoxicillin to prevent infective endocarditis in periodontitis patients reconsidered: a narrative review. *Swiss Med Weekly*. 2021;151:w30078. doi:10.4414/SMW.2021.w30078
3. Lockhart PB, Brennan MT, Thornhill M, et al. Poor oral hygiene as a risk factor for infective endocarditis-related bacteremia. *J Am Dent Assoc*. 2009;140(10):1238–1244. doi:10.14219/jada.archive.2009.0046
4. Bottino MC, Thomas V, Janowski GM. A novel spatially designed and functionally graded electrospun membrane for periodontal regeneration. *Acta Biomater*. 2011;7(1):216–224. doi:10.1016/j.actbio.2010.08.019
5. Bottino MC, Thomas V, Schmidt G, et al. Recent advances in the development of GTR/GBR membranes for periodontal regeneration—A materials perspective. *Dent Mater J*. 2012;28(7):703–721. doi:10.1016/j.dental.2012.04.022

6. Xiu W, Wan L, Yang K, et al. Potentiating hypoxic microenvironment for antibiotic activation by photodynamic therapy to combat bacterial biofilm infections. *Nat Commun*. 2022;13(1):3875. doi:10.1038/s41467-022-31479-x
7. Zhou X, Dong L, Zhao B, et al. A photoactivatable and phenylboronic acid-functionalized nanoassembly for combating multidrug-resistant gram-negative bacteria and their biofilms. *Burns Trauma*. 2023;11:tkad041. doi:10.1093/burnst/tkad041
8. Chen Y, Dai F, Deng T, et al. An injectable MB/BG@LG sustained release lipid gel with antibacterial and osteogenic properties for efficient treatment of chronic periodontitis in rats. *Materials Today Bio*. 2023;21:100699. doi:10.1016/j.mtbio.2023.100699
9. Huang X, Lou Y, Duan Y, et al. Biomaterial scaffolds in maxillofacial bone tissue engineering: a review of recent advances. *Bioact Mater*. 2024;33:129–156.
10. Groeger S, Zhou Y, Ruf S, Meyle J. Pathogenic mechanisms of Fusobacterium nucleatum on oral epithelial cells. *Front Oral Health*. 2022;3:831607. doi:10.3389/froh.2022.831607
11. Hofer U. Fusobacterium orchestrates oral biofilms. *Nat Rev Microbiol*. 2022;20(10):576.
12. Brennan CA, Garrett WS. Fusobacterium nucleatum - symbiont, opportunist and oncobacterium. *Nat Rev Microbiol*. 2019;17(3):156–166. doi:10.1038/s41579-018-0129-6
13. Harmata AJ, Ma Y, Sanchez CJ, et al. D-amino acid inhibits biofilm but not new bone formation in an ovine model. *Clin Orthop Relat Res*. 2015;473(12):3951–3961. doi:10.1007/s11999-015-4465-9
14. Warraich AA, Mohammed AR, Perrie Y, Hussain M, Gibson H, Rahman A. Evaluation of anti-biofilm activity of acidic amino acids and synergy with ciprofloxacin on staphylococcus aureus biofilms. *Sci Rep*. 2020;10(1):9021. doi:10.1038/s41598-020-66082-x
15. Zhao T, Chen J, Liu S, et al. Transcriptome analysis of Fusobacterium nucleatum reveals differential gene expression patterns in the biofilm versus planktonic cells. *Biochem Biophys Res Commun*. 2022;593:151–157. doi:10.1016/j.bbrc.2021.11.075
16. Lu J, Yu N, Liu Q, Xie Y, Zhen L. Periodontal ligament stem cell exosomes key to regulate periodontal regeneration by miR-31-5p in mice model. *Int j Nanomed*. 2023;18:5327–5342. doi:10.2147/IJN.S409664
17. Kim BC, Bae H, Kwon IK, et al. Osteoblastic/cementoblastic and neural differentiation of dental stem cells and their applications to tissue engineering and regenerative medicine. *Tissue Eng Part B Rev*. 2012;18(3):235–244. doi:10.1089/ten.teb.2011.0642
18. Kim SS, Kwon DW, Im I, et al. Differentiation and characteristics of undifferentiated mesenchymal stem cells originating from adult premolar periodontal ligaments. *Korean J Orthod*. 2012;42(6):307–317. doi:10.4041/kjod.2012.42.6.307
19. Huang GT, Gronthos S, Shi S. Mesenchymal stem cells derived from dental tissues vs. those from other sources: their biology and role in regenerative medicine. *J Dent Res*. 2009;88(9):792–806. doi:10.1177/0022034509340867
20. Zhang F, Allen AJ, Levine LE, et al. Structural and dynamical studies of acid-mediated conversion in amorphous-calcium-phosphate based dental composites. *Dent Mater J*. 2014;30(10):1113–1125. doi:10.1016/j.dental.2014.07.003
21. Stamboulis A, Hench LL, Boccaccini AR. Mechanical properties of biodegradable polymer sutures coated with bioactive glass. *J Mater Sci Mater Med*. 2002;13(9):843–848. doi:10.1023/A:1016544211478
22. Lee WH, Zavgorodniy AV, Loo CY, Rohanizadeh R. Synthesis and characterization of hydroxyapatite with different crystallinity: effects on protein adsorption and release. *J Biomed Mater Res Part A*. 2012;100A(6):1539–1549. doi:10.1002/jbm.a.34093
23. Wang Z, Liu X, Duan Y, Huang Y. Infection microenvironment-related antibacterial nanotherapeutic strategies. *Biomaterials*. 2022;280:121249. doi:10.1016/j.biomaterials.2021.121249
24. Kang S, Hou S, Chen X, et al. Energy-saving electrospinning with a concentric teflon-core rod spinneret to create medicated nanofibers. *Polymers*. 2020;12:10. doi:10.3390/polym12102421
25. Huang X, Jiang W, Zhou J, Yu DG, Liu H. The applications of ferulic-acid-loaded fibrous films for fruit preservation. *Polymers*. 2022;14:22. doi:10.3390/polym14224947
26. Wang Y, Yu DG, Liu Y, Liu YN. Progress of electrospun nanofibrous carriers for modifications to drug release profiles. *J Funct Biomater*. 2022;13:4. doi:10.3390/jfb13010004
27. Miele D, Ruggeri M, Vigani B, et al. Nanoclay-doped electrospun nanofibers for tissue engineering: investigation on the structural modifications in physiological environment. *Int j Nanomed*. 2023;18:7695–7710. doi:10.2147/IJN.S431862
28. Yu DG, Huang C. Electrospun biomolecule-based drug delivery systems. *Biomolecules*. 2023;13:7. doi:10.3390/biom13071152
29. He S, Wen H, Yao N, Wang L, Huang J, Li Z. A sustained-release nanosystem with mrsa biofilm-dispersing and -eradicating abilities accelerates diabetic ulcer healing. *Int j Nanomed*. 2023;18:3951–3972. doi:10.2147/IJN.S410996
30. Hedvičáková V, Žižková R, Buzgo M, et al. The gradual release of alendronate for the treatment of critical bone defects in osteoporotic and control rats. *Int j Nanomed*. 2023;18:541–560. doi:10.2147/IJN.S386784
31. Wang Z, Wu A, Cheng W, et al. Adoptive macrophage directed photodynamic therapy of multidrug-resistant bacterial infection. *Nat Commun*. 2023;14(1):7251. doi:10.1038/s41467-023-43074-9
32. Yu DG, Zhou J. How can electrospinning further service well for pharmaceutical researches? *J Pharmaceut Sci*. 2023;112(11):2719–2723. doi:10.1016/j.xphs.2023.08.017
33. Yu Q, Shen C, Wang X, Wang Z, Liu L, Zhang J. Graphene Oxide/Gelatin nanofibrous scaffolds loaded with n-acetyl cysteine for promoting wound healing. *Int j Nanomed*. 2023;18:563–578. doi:10.2147/IJN.S392782
34. Yadav S, Arya DK, Pandey P, et al. ECM mimicking biodegradable nanofibrous scaffold enriched with curcumin/ZnO to accelerate diabetic wound healing via multifunctional bioactivity. *Int j Nanomed*. 2022;17:6843–6859. doi:10.2147/IJN.S388264
35. Cheng J, Gan G, Zheng S, et al. Biofilm heterogeneity-adaptive photoredox catalysis enables red light-triggered nitric oxide release for combating drug-resistant infections. *Nat Commun*. 2023;14(1):7510. doi:10.1038/s41467-023-43415-8
36. Duan H, Chen H, Qi C, et al. A novel electrospun nanofiber system with PEGylated paclitaxel nanocrystals enhancing the transmucus permeability and in situ retention for an efficient cervicovaginal cancer therapy. *Int J Pharm*. 2024;650:123660. doi:10.1016/j.ijpharm.2023.123660
37. Lu Y, Huang J, Yu G, et al. Coaxial electrospun fibers: applications in drug delivery and tissue engineering. *Wiley Interdiscip Rev Nanomed Nanobiotechnol*. 2016;8(5):654–677. doi:10.1002/wnan.1391
38. Porter JR, Henson A, Popat KC. Biodegradable poly(epsilon-caprolactone) nanowires for bone tissue engineering applications. *Biomaterials*. 2009;30(5):780–788. doi:10.1016/j.biomaterials.2008.10.022
39. Chastain SR, Kundu AK, Dhar S, Calvert JW, Putnam AJ. Adhesion of mesenchymal stem cells to polymer scaffolds occurs via distinct ECM ligands and controls their osteogenic differentiation. *J Biomed Mater Res Part A*. 2006;78A(1):73–85. doi:10.1002/jbm.a.30686

40. Stoecklin-Wasmer C, Rutjes AW, da Costa BR, Salvi GE, Jüni P, Sculean A. Absorbable collagen membranes for periodontal regeneration: a systematic review. *J Dent Res*. 2013;92(9):773–781. doi:10.1177/0022034513496428
41. Xu X, Zhou Y, Zheng K, Li X, Li L, Xu Y. 3D Polycaprolactone/Gelatin-Oriented Electrospun scaffolds promote periodontal regeneration. *ACS Appl Mater Interfaces*. 2022;14(41):46145–46160. doi:10.1021/acsami.2c03705
42. Combes C, Rey C. Amorphous calcium phosphates: synthesis, properties and uses in biomaterials. *Acta Biomater*. 2010;6(9):3362–3378. doi:10.1016/j.actbio.2010.02.017
43. Ding GJ, Zhu YJ, Qi C, Lu BQ, Wu J, Chen F. Porous microspheres of amorphous calcium phosphate: block copolymer templated microwave-assisted hydrothermal synthesis and application in drug delivery. *J Colloid Interface Sci*. 2015;443:72–79. doi:10.1016/j.jcis.2014.12.004
44. Dorozhkin SV. Amorphous calcium (ortho)phosphates. *Acta biomaterialia*. 2010;6(12):4457–4475. doi:10.1016/j.actbio.2010.06.031
45. Pasupuleti RR, Tsai P-C, Ponnusamy VK. Low-cost disposable poly(ethyleneimine)-functionalized carbon nanofibers coated cellulose paper as efficient solid phase extraction sorbent material for the extraction of parahydroxybenzoates from environmental waters. *Chemosphere*. 2021;267:129274. doi:10.1016/j.chemosphere.2020.129274
46. Chen X, Wang J, An Q, et al. Electrospun poly(L-lactic acid-co-ε-caprolactone) fibers loaded with heparin and vascular endothelial growth factor to improve blood compatibility and endothelial progenitor cell proliferation. *Colloids Surf B Biointerfaces*. 2015;128:106–114. doi:10.1016/j.colsurfb.2015.02.023
47. Wang J, Chen Y, Li J, et al. Electrospun polysaccharides for periodontal tissue engineering: a review of recent advances and future perspectives. *Ann Biomed Eng*. 2022;50(7):769–793. doi:10.1007/s10439-022-02952-x
48. Muhammad Q, Jang Y, Kang SH, Moon J, Kim WJ, Park H. Modulation of immune responses with nanoparticles and reduction of their immunotoxicity. *Biomater Sci*. 2020;8(6):1490–1501. doi:10.1039/C9BM01643K
49. Wei J, Igarashi T, Okumori N, et al. Influence of surface wettability on competitive protein adsorption and initial attachment of osteoblasts. *Biomed Mater Res*. 2009;4(4):045002. doi:10.1088/1748-6041/4/4/045002
50. Rubini D, Farisa Banu S, Veda Hari BN, et al. Chitosan extracted from marine biowaste mitigates staphyloxanthin production and biofilms of methicillin- resistant staphylococcus aureus. *Food Chem Toxicol*. 2018;118:733–744. doi:10.1016/j.fct.2018.06.017
51. Wu C, Chen YW, Scheible M, et al. Genetic and molecular determinants of polymicrobial interactions in Fusobacterium nucleatum. *Proc Natl Acad Sci U S A*. 2021;118:23.
52. Xu W, Zhou W, Wang H, Liang S. Roles of porphyromonas gingivalis and its virulence factors in periodontitis. *Protein Chem Struct Biol*. 2020;120:45–84.
53. Morrison SJ, Scadden DT. The bone marrow niche for haematopoietic stem cells. *Nature*. 2014;505(7483):327–334. doi:10.1038/nature12984
54. Greenbaum A, Hsu Y-MS, Day RB, et al. CXCL12 in early mesenchymal progenitors is required for haematopoietic stem-cell maintenance. *Nature*. 2013;495(7440):227–230. doi:10.1038/nature11926
55. Chen J, Mo Q, Sheng R, et al. The application of human periodontal ligament stem cells and biomimetic silk scaffold for in situ tendon regeneration. *Stem Cell Res Ther*. 2021;12(1):596. doi:10.1186/s13287-021-02661-7
56. Staples RJ, Ivanovski S, Vaquette C. Fibre guiding scaffolds for periodontal tissue engineering. *J Periodontal Res*. 2020;55(3):331–341. doi:10.1111/jre.12729
57. Geurs NC, Korostoff JM, Vassilopoulos PJ, et al. Clinical and histologic assessment of lateral alveolar ridge augmentation using a synthetic long-term bioabsorbable membrane and an allograft. *J Periodontol*. 2008;79(7):1133–1140. doi:10.1902/jop.2008.070595
58. Zhang Y, Chen R, Wang Y, et al. Antibiofilm activity of ultra-small gold nanoclusters against Fusobacterium nucleatum in dental plaque biofilms. *J Nanobiotechnol*. 2022;20(1):470. doi:10.1186/s12951-022-01672-7
59. Ren S, Yao Y, Zhang H, et al. Aligned fibers fabricated by near-field electrospinning influence the orientation and differentiation of hPDLSCs for periodontal regeneration. *J Biomed Nanotechnol*. 2017;13(12):1725–1734. doi:10.1166/jbn.2017.2451